Calculation of kilovoltage beam radiotherapy ionization chamber correction factors

Julien Bancheri

Medical Physics Unit
McGill University, Montréal

September 2019

A thesis submitted to McGill University in partial fulfillment of the requirements of the degree of Master of Science

Abstract

Kilovoltage (kV) x-ray beams can be calibrated with the in-phantom method by determining the absorbed dose to water at a depth of 2 cm in a water phantom. The overall chamber correction factor accounts for changes in the chamber response due to the displacement of water by the chamber cavity and wall, the presence of the stem and the change in incident photon energy and angular distribution in the phantom to that in air. The effects of a waterproof sheath (if required) are accounted for in a sheath correction factor. The aim of this thesis is to calculate chamber correction factors through Monte Carlo simulations. They are compared to experimental values obtained at PTB with their recently-developed water calorimetry-based absorbed dose to water primary standard and other national metrological institutes. The simulations were carried out with EGSnrc which incorporated measured photon fluence spectra and renormalized photon cross sections. Models for the PTW TM30013, NE2571, IBA FC65-G, IBA FC65-P and Exradin A12 ionization chambers were based on manufacturer blueprints. The calculated chamber correction factors were all within 3% of unity. A detailed uncertainty analysis was carried out which considered the contributions to the uncertainty on the chamber correction factors from the field size, photon cross sections, photon fluence spectra and chamber wall and central electrode dimensions. The standard uncertainty on the calculated factors was determined to be 0.3%. For the 50 kV and 100-200 kV radiation beam qualities, the calculated correction factors deviate from the measured correction factors (with a standard uncertainty of 1%) by up to 2.7%. The calculated chamber correction factors for the PTW TM30013 and A12 are consistent with those calculated by the BIPM kilovoltage primary standard. The inconsistencies between the calculated and experimental chamber correction factors indicate the need to further investigate the accuracy of the absorbed dose to water primary standard and the use of Monte Carlo simulations to determine kilovoltage beam chamber correction factors.

Résumé

Les faisceaux kilovoltage (kV) de rayons x peuvent être calibrés avec la méthode in-phantom en déterminant la dose absorbée dans l'eau à une profondeur de 2 cm dans un fantôme d'eau. Le facteur de correction global de la chambre tient compte des changements dans la réponse de la chambre dus au déplacement de l'eau par la cavité et la paroi de la chambre, à la présence de la tige et au changement de la distribution énergétique et angulaire des photons incidents dans le fantôme par rapport à celle dans l'air. Les effets d'une gaine imperméable (si nécessaire) sont pris en compte dans un facteur de correction de gaine. Le but de cette thèse est de calculer les facteurs de correction de la chambre à l'aide de simulations de Monte Carlo. Ils sont comparés aux valeurs expérimentales obtenues chez PTB avec leur étalon primaire de dose absorbée dans l'eau à base de calorimétrie de l'eau récemment développée et à d'autres instituts de métrologie nationaux. Les simulations ont été effectuées avec EGSnrc, qui incorporait des spectres de fluence de photons mesurés et des sections efficaces de photons renormalisées. Les modèles des chambres d'ionisation PTW TM30013, NE2571, IBA FC65-G, IBA FC65-P et Exradin A12 étaient basés sur les plans du fabricant. Les facteurs de correction de la chambre calculés étaient tous à moins de 3% de l'unité. Une analyse d'incertitude détaillée a été réalisée. Elle a examiné les contributions à l'incertitude des facteurs de correction de la chambre à partir de la taille du champ, des sections efficaces de photons, des spectres de fluence de photons et des dimensions de la paroi de la chambre et de l'électrode centrale. L'incertitude standard sur les facteurs calculés a été établie à 0.3%. Pour les qualités de faisceau de rayonnement de 50 kV et 100-200 kV, les facteurs de correction calculés s'écartent des facteurs de correction mesurés (avec une incertitude standard de 1%) jusqu'à 2.7%. Les facteurs de correction de chambre calculés pour le PTW TM30013 et A12 sont cohérents avec ceux calculés par l'étalon primaire kilovoltage du BIPM. Les incohérences entre les facteurs de correction de la chambre calculés et expérimentaux indiquent qu'il est nécessaire d'étudier plus avant la précision de l'étalon primaire de dose absorbée dans l'eau et l'utilisation des simulations de Monte Carlo pour déterminer les facteurs de correction de la chambre dans les faisceaux kilovoltage.

Acknowledgements

I would like to thank and acknowledge the people that have supported and contributed to this thesis over its duration.

First and foremost, I would like to express my gratitude towards my supervisor Dr. Jan Seuntjens. Thank you for your patience and insight whenever I required it. My work and abilities as a researcher have greatly benefited from your support and confidence over the years.

I would like to extend my thanks to Dr. Ludwig Büermann and Dr. Steffen Ketelhut of PTB for the valuable data they provided me with and for the in-depth discussions about the results of this work and their interpretation.

I would like to thank Dr. Jan Würfel of PTW-Freiburg and Frantisek Gabris of IBA for ionization chamber blueprints.

I would like to acknowledge NSERC for funding this work.

Many thanks to the Margery Knewstubb and Tatjana Nisic, the unit secretaries, for all their help with administrative matters.

I would like to express my gratitude towards all family and friends that have supported me throughout my studies.

My thanks to all the staff and professors of the Medical Physics Unit, as well as my fellow students, for their help with this work.

Contents

6 Conclusion 100

Glossary

D Absorbed dose [Gy]. 5

$D_{w,z=2cm}$ Absorbed dose to water at a depth of 2 cm in a water phantom. 8

K_a Air kerma free-in-air. 8

$K_a^{in-water}$ Air kerma in a water phantom. 9

K_w Water kerma in a water phantom. 9

M_a Corrected ionization chamber reading free-in-air. 8

M_{raw} Raw ionization chamber reading [C]. 47

M_w Corrected ionization chamber reading at a depth of 2 cm in a water phantom. 9

$N_{D,w}$ Absorbed dose to water calibration coefficient. 10

N_K Air kerma calibration coefficient [$\frac{Gy}{C}$]. 8

$P_{Q,cham}$ Overall chamber correction factor. 8

P_{sheath} Waterproof sheath correction factor. 9

Φ Fluence [m^{-2}]. 34

Φ_E Fluence spectrum, fluence differential in energy [$J^{-1}\,m^{-2}$]. 34

Ψ Energy fluence [$J\,m^{-2}$]. 35

Ψ_E Energy fluence spectrum, energy fluence differential in energy $[m^{-2}]$. 35

$\frac{S_{el}}{\rho}$ Mass-electronic stopping power $\left[\frac{J\,m^2}{kg}\right]$. 26

$\frac{S_{rad}}{\rho}$ Mass-radiative stopping power $\left[\frac{J\,m^2}{kg}\right]$. 27

$\frac{S}{\rho}$ Mass stopping power $\left[\frac{J\,m^2}{kg}\right]$. 26

$\frac{\mu_{en}}{\rho}$ Mass-energy absorption coefficient $\left[\frac{m^2}{kg}\right]$. 25

$\frac{\mu_{tr}}{\rho}$ Mass-energy transfer coefficient $\left[\frac{m^2}{kg}\right]$. 25

$\frac{\mu}{\rho}$ Mass-linear attenuation coefficient $\left[\frac{m^2}{kg}\right]$. 24

$\frac{d\sigma}{d\Omega}$ Differential cross section $\left[\frac{m^2}{sr.}\right]$. 17

$\left[(\overline{\mu_{en}}/\rho)_{w,a}\right]_{w,Q,z=2cm}$ Water-to-air mass-energy absorption coefficient ratio averaged over the photon energy fluence spectrum at the reference point and at a depth of 2 cm in a water phantom in the absence of a ionization chamber. 9

σ Total cross section [m^2]. 17

AAPM American Association of Physicists in Medicine. 7

BIPM International Bureau of Weights and Measures. 87

CPE Charged particle equilibrium. 9, 36

Gy Gray. 5

IAEA International Atomic Energy Agency. 7

IPEMB Institution of Physics and Engineering in Medicine and Biology. 7

Kerma Kinetic energy released per unit mass $[Gy]$. 35

linac Linear Accelerator. 5, 29

NCS Nederlandse Commissie voor Stralingsdosimetrie. 7

PSDL Primary Standards Dosimetry Laboratory. 6

PTB Physikalisch-Technische Bundesanstalt. 11

TCPE Transient charged particle equilibrium. 37

List of Figures

List of Tables

Chapter 1

Introduction

1.1 Cancer statistics and treatment

Cancer is the second leading cause of death worldwide and is responsible for an estimated 9.6 million deaths worldwide per year [1]. In Canada, it is the leading cause of death. Approximately one in two Canadians will develop cancer in their lifetime and one in four will be expected to die from such causes [2]. Relative to 1988, the total number of new cancer cases has increased twofold to about 100,000 in 2017 (for both sexes) [3]. The total number of deaths has also increased since 1988 to about 40,000 (both sexes). These statistics can be understood by considering population growth and an increasingly aged population. This can be seen by the fact that 89% of diagnosed new cancer cases occur in Canadians that are over 50 years in age. Despite these numbers, the incidence and mortality rates (per 100,000) for Canadians of both sexes and all ages have decreased or stabilized in comparison to 1988. This can be attributed to healthier lifestyle habits, widespread knowledge of carcinogens, nation-wide cancer screening programs and improved cancer detection and treatment methods. For example, more than 80% of female breast cancer cases were diagnosed between stages I and II (early stages). Increasing rates can be seen when focusing in on specific age groups or sexes. The distribution of types of cancer by age group vary from children (0-14 years) to adolescents and young adults (15-29 years) and to adults (over 30 years) [3]. The prevalence of this disease in modern society has led to enormous efforts in research and research funding campaigns. In 2017, over $ 46 million has been invested in Canadian cancer research for all types [4].

There are multiple methods available for the treatment of cancer. The optimal treatment differs from patient to patient. The most well-known and most often used treatment options are surgery, chemotherapy and radiation therapy. The goal of surgery is to completely remove the tumour. Surgery is an extremely effective option during the early stages of cancer development and when there are no metastases. In cases where only partial tumour removal is possible, surgery itself is not possible or additional/concurrent therapy is required, other treatment options may be used either alone or in addition to surgery. Chemotherapy is one such option. During chemotherapy, drugs are given to the patient to destroy cancer cells or prevent their growth and spread. The decision of which chemotherapy drug(s) to use depends on several factors relating to the cancer (site, type, stage) and patient. Finally, radiotherapy is a treatment option which uses ionizing radiation to damage a cancer cell's DNA. Other treatment options do exist (e.g., hormonal therapies depending on tumor cell receptor status) but are less used and may still be in the research phase. Targeted therapy, a form of drug therapy that targets certain receptors occurring on some cancer cells, and immunotherapy are promising [5]. Note that the treatment goal may not always be to cure the disease. Control of the cancer's spread and growth, prevention and palliative care are alternative goals.

1.2 Radiation therapy

As mentioned above, radiation therapy is a form of cancer treatment that uses ionizing radiation. Due to this type of radiation's ability to liberate atomic orbital electrons, it is designated as *ionizing*. From this point on wards, ionizing radiation will simply be referred to as radiation. Ionizing radiation is further classified according to how the radiation causes energy to be deposited in a given medium. This deposited energy per unit mass is known as *absorbed dose*. Absorbed dose will be defined rigorously in Section 1.3. *Directly ionizing radiation* consists of charged particles such as electrons, protons and heavy ions (carbon, oxygen, etc.). A charged particle undergoes multiple interactions (hundreds to thousands of them) with the atoms of the medium. In each interaction some of the charged particle's kinetic energy is lost through excitation/ionization of the atom. It is in this sense that the charged particle *deposits* energy in the medium. *Indirectly ionizing radiation* consists of neutral particles such as photons and neutrons. This type of radiation deposits energy in the medium through a two-step process. First, the uncharged particle interacts with an orbital electron, transferring it some or all of it's energy. Secondly, the liberated electron, which is often called a *secondary* electron, deposits energy in the same manner as mentioned above. Uncharged and charged particles undergo quite different interactions and will be discussed further in Chapter 2.

The main reason radiation is an effective form of cancer treatment is because the radiation-medium interactions mentioned above can occur for a cancer cell's constituent atoms and molecules. These interactions manifest as biological damage to the cell and can even cause cell death. Damage to the cell's DNA by radiation is the main reason the cell has a biological response to radiation. The DNA is damaged through two separate mechanisms initiated by radiation. In *direct action*, the radiation interacts directly with the DNA. This mechanism often occurs for radiation types that deposit a large amount of energy in short distances (low energy electrons, protons, heavy ions). *Indirect action* occurs when the radiation interacts in the cellular DNA's surrounding environment. This environment is mostly water because water accounts for about 70% of the cell's total mass. Indirect action is a multi-step process. The electrons that are liberated by the radiation produce free radials through their interactions with the water molecules. Free radicals, such as ionized H_2O (H_2O^+), hydroxyl (OH) and hydrated electrons (e^-_{aq}), are a reactive species and can cause damage to the cellular DNA [6]. Indirect action is the main damage mechanism for photons. The cellular DNA is damaged when a single or both strands are broken. These breaks are known as single strand breaks and double strand breaks, respectively. The radiation damage to a cell will not always be lethal. If so, the damage can be repaired by the cell's various DNA repair mechanisms. The amount of damage caused by radiation depends on several factors. The cell is more sensitive to radiation (radiosensitive) during the mitosis (M phase) and G_2 periods of the cell cycle and more resistant (radioresistant) during the late period of DNA synthesis (S phase) [6]. Increased amounts of oxygen also cause the cell to be more radiosensitive. To take advantage of these biological factors, the total dose delivered to a patient will be spread out over time. This is known as fractionation.

Just as cancer cells can be damaged by radiation, so can healthy, normal tissues be damaged. Thus, any radiation therapy treatment must aim to minimize the amount of radiation normal tissues receive (sparing). This consideration forms a basis for the entire radiation therapy treatment workflow. Radiotherapy imaging and treatment planning define tumour volumes, organs at risk, which radiation types and energies will be used, how the radiation fields will be delivered (angles, distances, shapes, times, etc.) and dose profiles.

Radiation for medical purposes is produced by specialized machines such as x-ray tubes or linear accelerators (linac). These machines will be discussed in Section 2.5.

1.3 Radiation dosimetry

In radiation therapy, accurate knowledge of the radiation dose delivered to the patient is essential. Without accurate knowledge, the tumour site may receive too large or too small a dose. This holds for any normal tissues as well. This is where the field of radiation dosimetry plays its part. Radiation Dosimetry is the field that deals with quantification of radiation dose, mostly as a result of measurement using a device. Such a device that measures dose is known as a *radiation dosimeter*. Absorbed dose [Gy] is defined as

$$D = \frac{\mathrm{d}\bar{\epsilon}}{\mathrm{d}m}, \tag{1.1}$$

where D is the absorbed dose, $\mathrm{d}\bar{\epsilon}$ is the mean energy imparted by radiation to matter of a mass $\mathrm{d}m$ [7]. Note that absorbed dose is a scalar function of position in a medium. The SI unit of dose is Gray (Gy) which is 1 J/kg (Joule per kilogram). Water is chosen as the medium because it is similar enough to normal human tissues. For this reason, in clinical settings, absorbed dose to water is the quantity of interest; in radiation protection other quantities and media are also used.

The focus of this thesis will be on a type of dosimetry performed in the clinic known as *reference dosimetry*. The aim of reference dosimetry is to establish the absorbed dose to water per monitor unit (MU, a measure of treatment time) at a reference point in water under reference conditions. These conditions specify the reference depth of the reference point in water, the reference point's distance from the source and the radiation field's field size at a distance from the source. Reference conditions also specify the ambient temperature and pressure, which is usually Standard Ambient Temperature and Pressure (SATP, 298.15 K/22°C and 101.3 kPa). Reference dosimetry measurements are typically done in a large water tank known as a water phantom. The dosimeter is placed in the water phantom and the measurements are taken under reference conditions. The dosimeter is usually an air-filled ionization chamber. The operating principles of ionization chambers will be discussed in Section 3.3.

Dosimeters used in the clinical setting cannot measure absorbed dose to water directly. A conversion between the absorbed dose to water and the quantity the dosimeter registers is required. To determine this conversion, more commonly known as an *absorbed dose to water calibration coefficient*, the dosimeter needs to be calibrated against a radiation *primary standard*. A radiation primary standard is an instrument that is able to measure a quantity directly with low uncertainty and it's operation is independent of other instruments measuring the same quantity. An absorbed dose to water radiation primary standard measures absorbed dose to water and an air kerma radiation primary standard measures air kerma free-in-air. Water and graphite based calorimeters are often used as absorbed dose to water primary standards and free-air chambers as air kerma primary standards (see Section 3.4). The calibration of dosimeters occurs at a Primary Standards Dosimetry Laboratory (PSDL). Both the clinical dosimeter measurements and the primary standard measurements are done at the PSDL. The measurements are done under reference conditions and for a known reference radiation field/source. A key part of clinical reference dosimetry is that any calibrated dosimeter can be traced back to a PSDL and a primary standard.

1.4 Kilovoltage (kV) beam reference dosimetry

Roughly speaking, photon beams can be split into two energy regimes; kilovoltage (kV) beams and megavoltage (MV) beams. Megavoltage photon beams, which are produced by medical linacs, are made up of photons with energies in the MeV range. Although the large majority of radiation therapy is in MV beams, they do not play a role in the present work and will not be discussed much further. Kilovoltage beams are produced by x-ray tubes and have energies in the keV range. A kilovoltage beam is specified by its half value layer and tube potential (see Section 3.5). Kilovoltage beams can be further classified into two energy regimes. *Low energy* x-ray beams have a tube potential between 40 and 100 kV while *medium energy* x-ray beams have a tube potential between 100 and 300 kV.

Codes of practice or protocols for kilovoltage beam reference dosimetry are offered by the International Atomic Energy Agency (IAEA) TRS-398 [8], the American Association of Physicists in Medicine (AAPM) TG-61 [9], the Institution of Physics and Engineering in Medicine and Biology (IPEMB) [10] and the Nederlandse Commissie voor Stralingsdosimetrie (NCS) Report 10 [11]. All of them are based on the use of air-filled ionization chambers as the dosimeter of choice. The TRS-398 protocol is an absorbed dose to water-based protocol. This means ionization chambers are calibrated against an absorbed dose to water primary standard. The TG-61 protocol and others, on the other hand, are air kerma-based protocols. This means ionization chambers are calibrated against an air kerma primary standard (see Section 3.4). Kerma is a dosimetric concept that quantifies the amount of energy transferred to charged particles by uncharged particles (see Section 3.1), in this case photons. Air kerma primary standards are used because of the lack of absorbed dose to water primary standards for kilovoltage beams. Because of the absence of absorbed dose standards for low-energy photon beams at the time, the TRS-398 also offers air kerma-based calibration methods in these beams, identical to the TG-61.

The work done in this thesis is directly related to the above protocols so the reference dosimetry method of interest is presented here. In this method, called the *in-phantom method*, the absorbed dose to water at a depth of 2 cm in a water phantom on the central beam axis, $D_{w,z=2cm}$, is determined. The reference depth of this method is 2 cm in a water phantom. This method is recommended to be used with medium energy x-ray beams. A user's ionization chamber is first sent to a PSDL to be calibrated in terms of air kerma free-in-air, K_a. The beam under which the chamber is calibrated is similar to the user's beam in terms of the radiation beam quality specifiers, half value layer and tube potential (see Section 3.5). The air kerma calibration coefficient, N_K, is then

$$N_K = \frac{K_a}{M_a}, \tag{1.2}$$

where M_a is the ionization chamber reading in air corrected for temperature, pressure, ion recombination and polarity effects 3.3.2. The reading of an ionization chamber is in units of charge (Coulomb, C). The calibration coefficient is therefore given in units of Gy/C and converts charge to air kerma. For use in a water phantom at the reference depth, the air kerma calibration coefficient must be corrected for

- the change in incident photon energy and angular distribution in the water phantom to that in air.
- the presence of the chamber stem.
- the displacement of water by the chamber cavity and wall.

These corrections are contained in a single factor, the overall chamber correction factor $P_{Q,cham}$. This chamber correction factor is dependent on the type of ionization chamber and the radiation beam quality Q[1]. Some chambers are not waterproof and require a waterproof sheath. The correction to the calibration coefficient for the sheath is contained in P_{sheath}. Note that P_{sheath} is unity if the chamber is waterproof. The air kerma in the water phantom at the reference depth of 2 cm, $K_a^{in-water}$, is then

$$K_a^{in-water} = M_w N_K P_{Q,cham} P_{sheath} \ , \tag{1.3}$$

where M_w is the corrected chamber reading now at a depth of 2 cm in the water phantom. Air kerma in water is converted to water kerma (in water), K_w, through the water-to-air mass-energy absorption coefficient ratio averaged over the photon energy fluence spectrum at the reference point in the water phantom in the absence of the chamber, $\left[(\overline{\mu_{en}}/\rho)_{w,a}\right]_{w,Q,z=2cm}$, i.e.,

$$K_w = K_a^{in-water} \left[\frac{(\overline{\mu_{en}}/\rho)_{water}}{(\overline{\mu_{en}}/\rho)_{air}}\right]_{w,Q,z=2cm} = K_a^{in-water} \left[\left(\frac{\overline{\mu_{en}}}{\rho}\right)_{w,a}\right]_{w,Q,z=2cm} \tag{1.4}$$

The factor $\left[(\overline{\mu_{en}}/\rho)_{w,a}\right]_{w,Q,z=2cm}$ is chamber independent but does depend on the field size of the beam, the beam quality Q and the reference depth. In Equation 1.4, the assumption that the radiative losses of electrons are negligible (see Sections 2.3.2 and 2.4) is made. This holds for low energy photons in general. Therefore, there is a negligible difference between the kerma and the electronic kerma (see Section 3.1). With this assumption and the assumption of the existence of charged particle equilibrium (CPE, see Section 3.1), the absorbed dose to water at the reference depth is approximately water kerma, i.e.,

---

[1] The overall chamber correction factor is, in principle, dependent on the radiation field spectrum at the point of measurement and hence also dependent on field size, i.e., scattering conditions.

$$D_{w,z=2cm} \approx K_w = M_w N_K \left[\left(\frac{\overline{\mu_{en}}}{\rho} \right)_{w,a} \right]_{w,Q,z=2cm} P_{Q,cham} P_{sheath} \tag{1.5}$$

Note how, by dividing $D_{w,z=2cm}$ by M_w, the absorbed dose to water calibration coefficient $N_{D,w}$ is

$$N_{D,w} = N_K \left[\left(\frac{\overline{\mu_{en}}}{\rho} \right)_{w,a} \right]_{w,Q,z=2cm} P_{Q,cham} P_{sheath}. \tag{1.6}$$

1.5 Thesis motivation and goals

In absence of primary standards for absorbed dose to water, the factors $P_{Q,cham}$, $\left[(\overline{\mu_{en}}/\rho)_{w,a} \right]_{w,Q,z=2cm}$ and P_{sheath} are very difficult to measure in practice. Over the past few decades, they have mostly been determined through pure Monte Carlo (MC) simulations or a mix of simulations and experiments. The overall chamber correction factor $P_{Q,cham}$, has been especially under-investigated.

Early dosimetry protocols, such as the ICRU Report 23 [12], acknowledged the presence of a chamber-dependent correction factor but had no data available. Schneider *et. al.* demonstrated the necessity of such a chamber-dependent correction factor that varied with radiation beam quality [13]. Several subsequent studies, now two decades old, were conducted on determining the overall chamber correction factor [14–17]. These studies employed a mix of ionization chamber measurements and Monte Carlo simulations. The Monte Carlo codes used in these investigations (EGS4) are now considered out of date in comparison to modern day radiation transport Monte Carlo codes such as EGSnrc (see Section 4.2). The new MC codes include improved physics (multiple scattering, photon interactions, electron interactions, atomic relaxations, spin effects), electron transport algorithms, variance reduction techniques and new user codes (applications) all together. The overall chamber correction factors calculated with these old Monte Carlo codes are published in the codes of practice presented above and have not been updated since. These previously published chamber correction factors (and water-to-air mass-energy absorption coefficient ratios) are also outdated in terms of the photon and electron interaction data used in their calculation. The ICRU Report 90 [18], published in 2016, provides new data for electron stopping powers and photon cross sections. Updated values for the mean excitation energy of liquid water, dry air and graphite and the density effect correction for graphite result in updated electron stopping powers. The ICRU Report 90 also offers a variety of data sets for each photon interaction cross section. Special attention is given to the photoelectric interaction cross section (explained further in Section 2.2.1). The influence of these updates on kilovoltage beam chamber correction factor calculations has yet to be explored.

Investigations into kilovoltage beam chamber correction factors have also been held back due to lack of absorbed dose to water primary standards for kilovoltage beams. Initial investigations into water calorimetry-based kilovoltage beam dosimetry had been performed by Kubo [19], Mattsson [20] and Seuntjens *et. al.* [14] but at the time of release of the codes of practice, no kilovoltage beam absorbed dose to water primary standard was available. Only recently has this changed with the development of kilovoltage beam absorbed dose to water primary standards in Europe [21–24]. Such developments have renewed the interest in kilovoltage beam dosimetry and allow for the direct measurement of kilovoltage beam chamber correction factors. The German national metrology institute Physikalisch-Technische Bundesanstalt (PTB) has obtained experimental values for chamber correction factors with their recently-developed water calorimetry-based absorbed dose to water primary standard. Validation for Monte Carlo calculated chamber correction factors can be established through comparisons with these experimental factors. An update to the IAEA TRS-398 is being developed which aims to include these newly determined chamber correction factors.

The main aim of this thesis is to calculate new kilovoltage beam chamber correction factors for use with the in-phantom method. This work is done in the context of the IAEA TRS-398 update, the ICRU Report 90, up-to-date Monte Carlo codes (EGSnrc) and the development of kilovoltage beam absorbed dose to water primary standards. The three specific aims of this thesis are

1. Calculate new kilovoltage beam chamber correction factors using up-to-date Monte Carlo and photon and electron interaction data for the PTW TM30013, NE2571, IBA FC65-G, IBA FC65-P and Exradin A12 ionization chambers.
2. Compare the calculated chamber correction factors to the experimental values obtained at PTB with their recently-developed water calorimetry-based absorbed dose to water primary standard.
3. Perform a detailed uncertainty analysis on the calculated chamber correction factors.

References

1. World Health Organization. *Cancer.* (World Health Organization, 2018). https://www.who.int/news-room/fact-sheets/detail/cancer.
2. Canadian Cancer Society's Advisory Committee on Cancer Statistics. *Canadian Cancer Statistics.* (Canadian Cancer Society, Toronto, Canada, 2018). https://www.cancer.ca/~/media/cancer.ca/CW/cancer%20information/cancer%20101/Canadian%20cancer%20statistics/Canadian-Cancer-Statistics-2018-EN.pdf?la=en.
3. Canadian Cancer Society's Advisory Committee on Cancer Statistics. *Canadian Cancer Statistics.* (Canadian Cancer Society, Toronto, Canada, 2017). https://www.cancer.ca/~/media/cancer.ca/CW/cancer%20information/cancer%20101/Canadian%20cancer%20statistics/Canadian-Cancer-Statistics-2017-EN.pdf?la=en.

4. Canadian Cancer Society. *Our Research Impact.* (Canadian Cancer Society, Toronto, Canada, 2017). http://www.cancer.ca/~/media/Research/2018/Research%20Impact%20Brochure/2017_Research-Impact-Brochure_EN.pdf?la=en.
5. Garassino, M. *Personalised Cancer Medicine: An ESMO Guide for Patients.* (European Society for Medical Oncology, Lugano, Switzerland, 2013). https://www.esmo.org/content/download/20122/337223/file/ESMO-Patient-Guide-Personalised-Cancer-Medicine.pdf.
6. International Atomic Energy Agency. *Radiation Biology: A Handbook for Teachers and Students.* (IAEA, Vienna, Austria, 2010).
7. Report 85. *Journal of the International Commission on Radiation Units and Measurements* **11(1),** NP (2011).
8. IAEA. *Absorbed Dose Determination in External Beam Radiotherapy: An International Code of Practice for Dosimetry Based on Standards of Absorbed Dose to Water. Techincal Report Series* **398** (IAEA, Vienna, Austria, 2001).
9. Ma, C.-M. *et al.* AAPM protocol for 40–300 kV x-ray beam dosimetry in radiotherapy and radiobiology. *Medical Physics* **28(6),** 868–893 (2001).
10. Prepared by a Working Party of the (Chair) and Aukett, R. J., Harrison, R. M., Moretti, C., Nahum, A. E. & Rosser, K. E. The IPEMB code of practice for the determination of absorbed dose for x-rays below 300 kV generating potential (0.035 mm Al - 4 mm Cu HVL; 10 - 300 kV generating potential). *Physics in Medicine and Biology* **41(12),** 2605–2625 (1996).
11. Grimbergen, T. W. M. *et al. NCS Report 10: Dosimetry of low and medium energy X-rays* **10** (NCS, Delft, The Netherlands, 1997).
12. ICRU. Report 23. *Journal of the International Commission on Radiation Units and Measurements* **os12(2)** (1973).

13. Schneider, U., Grosswendt, B. & Kramer, H. M. *Perturbation correction factor for x-rays between 70 and 280 kV* in *Dosimetry in Radiotherapy: Proceedings of an International Symposium on Dosimetry in Radiotherapy* **vol 1** (IAEA, Vienna, Austria, 1988), 141–148.

14. Seuntjens, J., Thierens, H. & Schneider, U. Correction factors for a cylindrical ionization chamber used in medium-energy X-ray beams. *Physics in Medicine and Biology* **38(6),** 805–832 (1993).

15. Seuntjens, J. & Verhaegen, F. Dependence of overall correction factor of a cylindrical ionization chamber on field size and depth in medium-energy x-ray beams. *Medical Physics* **23(10),** 1789–1796 (1996).

16. Ma, C.-M. & Nahum, A. E. Monte Carlo calculated stem effect corrections for NE2561 and NE2571 chambers in medium-energy X-ray beams. *Physics in Medicine and Biology* **40(1),** 63–72 (1995).

17. Ma, C.-M. & Nahum, A. E. Calculations of ion chamber displacement effect corrections for medium-energy X-ray dosimetry. *Physics in Medicine and Biology* **40(1),** 45–62 (1995).

18. Seltzer, S. M. *et al.* ICRU Report 90. Key data for ionizing-radiation dosimetry: Measurement standards and applications. *Journal of the International Commission on Radiation Units and Measurements* **14(1)** (2016).

19. Kubo, H. Water calorimetric determination of absorbed dose by 280 kVp orthovoltage X-rays. *Radiotherapy and Oncology* **4(3),** 275–281 (1985).

20. Mattsson, L. O. Comparison of water calorimetry and ionization chamber dosimetry in 100 and 200 kV x-ray beams. *CCEMRI(1),* 85 (1985).

21. De Prez, L. A. & de Pooter, J. A. The new NMi orthovolt x-rays absorbed dose to water primary standard based on water calorimetry. *Physics in Medicine and Biology* **53(13),** 3531–3542 (2008).

22. Krauss, A., Büermann, L., Kramer, H. M. & Selbach, H. J. Calorimetric determination of the absorbed dose to water for medium-energy x-rays with generating voltages from 70 to 280 kV. *Physics in Medicine and Biology* **57(19),** 6245–6268 (2012).

23. Rapp, B. *et al.* The LNE-LNHB water calorimeter for primary measurement of absorbed dose at low depth in water: application to medium-energy x-rays. *Physics in Medicine and Biology* **58(9),** 2769–2786 (2013).

24. Pinto, M. *et al.* A graphite calorimeter for absolute measurements of absorbed dose to water: application in medium-energy x-ray filtered beams. *Physics in Medicine and Biology* **61(4),** 1738–1764 (2016).

Chapter 2

Radiation Physics

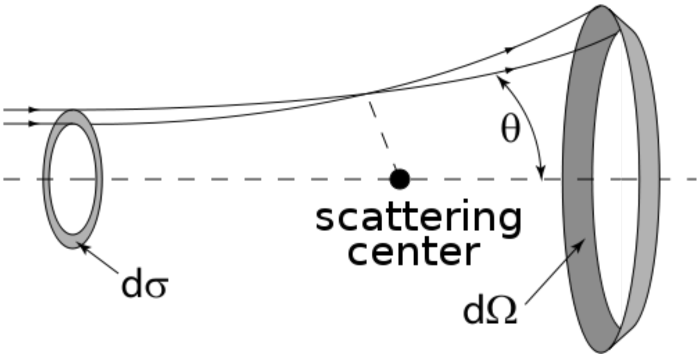

Figure 2.1 – Particles with a total cross section $d\sigma$ scatter into the solid angle $d\Omega$ with a scattering angle θ. The angle ϕ, as seen in Equation 2.2, revolves around the horizontal axis. The angular distribution about ϕ is often uniform. Taken from [25].

2.1 Cross sections

Incident charged and uncharged particles interact with the atoms of the medium they travel through. The probability of an incident particle undergoing an interaction is proportional to the *total cross section*, denoted as σ. The definition of a cross section is [7]

$$\sigma = \frac{\text{number of particles that have interacted / unit time}}{\text{number of incident particles / unit time / unit area}}. \tag{2.1}$$

Due to this definition, the SI units of the total cross section is m^2. Often times it is given in barns, b ($1\ \mathrm{b} = 10^{-28}\ \mathrm{m}^2$). As particles interact, they are scattered with certain scattering angles. This can be seen in Figure 2.1. The angular distribution of particles that have interacted is given by the *differential cross section*, $\frac{d\sigma}{d\Omega}$, such that,

$$\sigma = \int \frac{d\sigma}{d\Omega} d\Omega = \int \frac{d\sigma}{d\Omega} \sin\theta d\theta d\phi. \tag{2.2}$$

The total and differential cross section are microscopic quantities. They contain information for a single incident particle (of a given energy) and a single scatterer. This scatterer may be an orbital electron, nucleus, atom, etc. In the context of this thesis, the term cross section will

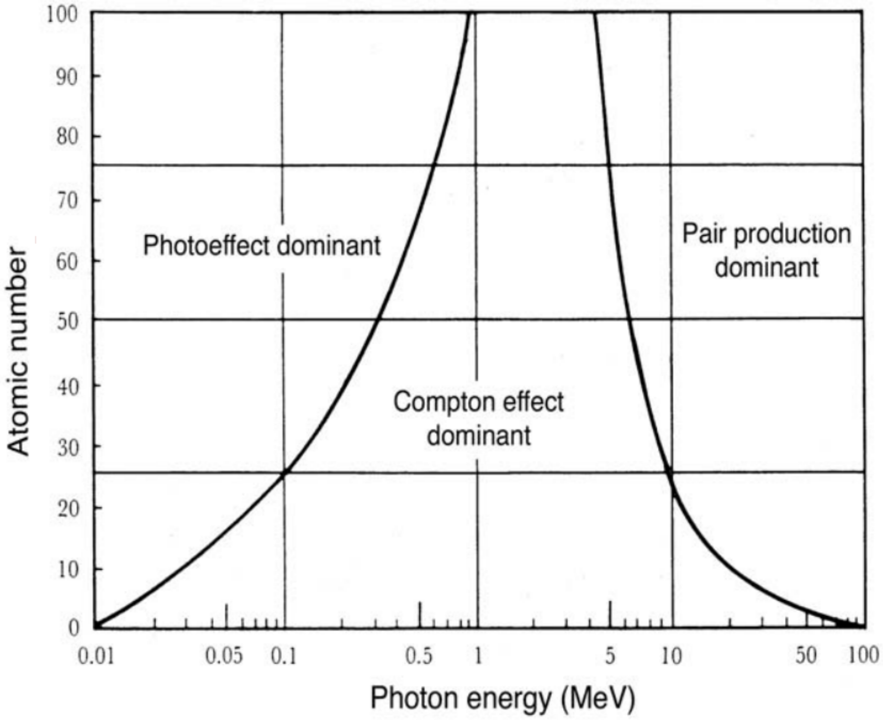

Figure 2.2 – The energy ranges where each photon interaction dominates. The black lines indicate where one interaction's atomic cross section is equal to the adjacent interaction's atomic cross section. As the atomic number increases, the photoelectric effect dominates at higher energies in comparison to lower atomic numbers. Adapted from [26].

imply atomic cross section unless otherwise specified. The analogous macroscopic quantities for photons are presented in Section 2.3.

2.2 Photon interactions

Photons can undergo several different interactions. These interactions fundamentally determine how a given photon beam behaves in a medium and how dose is deposited. Each interaction also has a greater or lower probability of occurring (at a given photon energy) based on the relative magnitudes of the individual interaction cross sections. Figure 2.2 shows the energy ranges where each photon interaction is dominant.

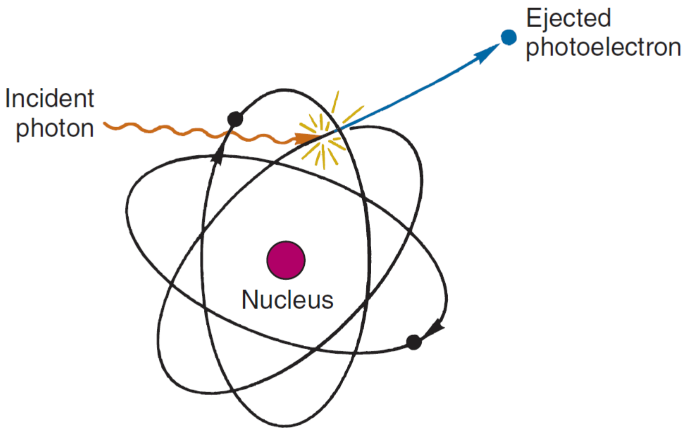

Figure 2.3 – The photoelectric interaction. Adapted from [27].

2.2.1 Photoelectric effect

The photoelectric effect is the most likely type of photon interaction to occur for low energy photons, below 100 keV for low atomic number elements. Materials seen in radiation dosimetry (water, air, graphite) generally have low atomic numbers. In this interaction, an incident photon is absorbed by an atom. Upon absorption of the photon, an orbital electron gains sufficient energy to overcome the binding energy of the orbital. The electron (photoelectron) is ejected from the atom and freely travels through the medium. A simplified diagram of this process is shown in Figure 2.3. Due to the ejection of an electron, relaxation processes follow a photoelectric interaction and energy may be emitted in the form of radiation or electrons emanating from the atom.

The direction of ejection of the photoelectrons is distributed according to a Sauter distribution [28]. The most probable direction of ejection increasingly deviates from the forward direction (the direction of travel of the incident photon) as the incident photon energy decreases. The photoelectric cross section σ_{PE} generally follows the relation

$$\sigma_{PE} \propto \frac{Z^n}{k^{7/2}}, \tag{2.3}$$

where Z is the atomic number, n is a number between 4 and 5 and k is the incident photon energy. This relation does not hold near absorption edges where a fine structure is exhibited. The strong atomic number dependence can be seen in Equation 2.3. The photon energy dependence of the cross section does change near absorption edges and low photon energies. Each atomic shell has its own photoelectric cross section as well. The total atomic cross section can be obtained by summing over the shell-wise cross sections. The K shell cross section is the largest relative to the other shells.

A subject of recent debate addressed in the ICRU Report 90 [18] is the accuracy of two published sets of photoelectric cross sections. The two "competing" data sets are referred to as renormalized or non-renormalized and are based upon different atomic models. The non-renormalized photoelectric sub-shell cross sections, for each atomic element, differ from the renormalized ones by an energy independent factor. This factor is the ratio of the electron densities near the nucleus predicted by each atomic model. Renormalized data sets were first compiled by [29] and later by Sabbatucci & Salvat [30]. The details of the theories are not relevant for this thesis and not discussed any further (see ICRU Report 90 for more details). For several decades, until recently, the non-renormalized cross sections were considered to be in better agreement with experiments [31, 32]. Experiments done at PTB in 2006 provided evidence that the renormalized cross sections were more accurate [33]. Both data sets are now available in radiation transport Monte Carlo codes, including EGSnrc 4.2.

2.2.2 Compton scattering

Compton scattering occurs when a photon interacts inelastically with an orbital electron. The energy that the incident photon loses in this interaction is transferred to an electron which is ejected from the atom (given that the energy transferred is larger than the binding energy). Due to ionization, relaxation processes follow this interaction. Compton scattering

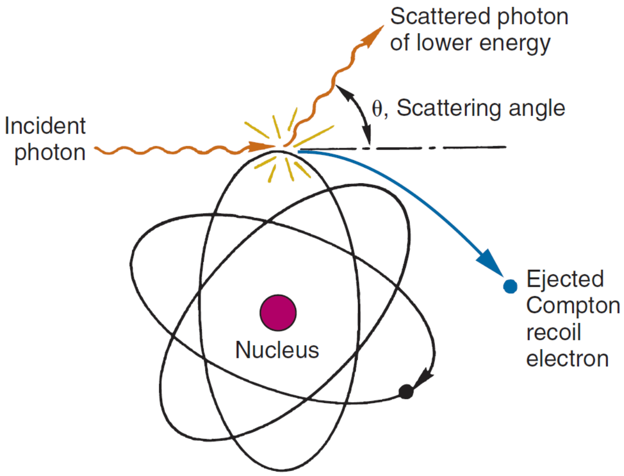

Figure 2.4 – An illustration of Compton scattering. Adapted from [27]

is the dominant photon interaction for photon energies above 100 keV for low atomic numbers.

Several theories exist which describe Compton scattering and it's cross section. The Klein-Nishina cross section is the most well-known Compton cross section and only considers an unbounded (free) and at-rest electron [34]. The relativistic impulse approximation (RIA) assumes that electrons in a given shell are free but move within a momentum distribution [35]. Each shell therefore has its own cross section. This formulation of Compton scattering is more accurate in that it takes into account Doppler broadening (electrons are not at rest) and binding effects. The double differential Compton cross section with the RIA approximation is given by

$$\frac{d^2\sigma_C}{dk'd\Omega} = \frac{r_e^2}{2}\frac{k'}{k}\frac{m_e}{q}\left[1 + \left(\frac{p_z}{m_e c}\right)^2\right]^{-1/2} X J(p_z) \tag{2.4}$$

where

$$J(p_z) = \iint \rho(\mathbf{p}) dp_x dp_y, \tag{2.5}$$

is the so-called Compton profile. In Equation 2.4, k is the incident photon energy, k' is the scattered photon energy, r_e is the classical electron radius, q is photon momentum transfer, p_z is the projection of q on the initial electron momentum vector, X is a function of these variables and scattering angle and $\rho(\mathbf{p})$ is the electron momentum distribution. The atomic number dependence of the Compton cross section is mostly contained within the Compton profile $J(p_z)$. Above 100 keV, the energy dependence of the cross section varies with energy as $1/k$. Below 100 keV, the Compton cross section increases with increasing energy.

2.2.3 Rayleigh scattering

Rayleigh scattering is the elastic scattering of a photon by an atom. The atom absorbs the incident photon and a photon of the same energy is re-emitted. As such, no energy is transferred to electrons. Rayleigh scattering occurs only at low photon energies. Considering just the photoelectric or Compton energy regimes, Rayleigh scattering is never the dominant interaction. The Rayleigh atomic differential cross section can be written as

$$\frac{d\sigma_R}{d\Omega} = r_e^2 \frac{1+\cos^2\theta}{2} \left|F(\mathbf{q},Z) + f' + if''\right|^2 , \tag{2.6}$$

where θ is the photon scattering angle and $F(\mathbf{q},Z)$ is the atomic form factor with $\mathbf{q}$ being the photon momentum transfer vector. The atomic form factor accounts for the constructive and destructive interference of the plane waves emitted by all of the electrons in the atom after absorbing the incident photon (plane wave). The quantity $f' + if''$ is the anomalous scattering factor which accounts for photon absorption near the absorption edges. The atomic number dependence of Rayleigh scattering is approximately Z^2. At photon energies near 1 keV, the Rayleigh total cross section is constant (Thomson scattering). As the photon energy increases, the energy dependence of the Rayleigh cross section goes like k^{-2}, k being

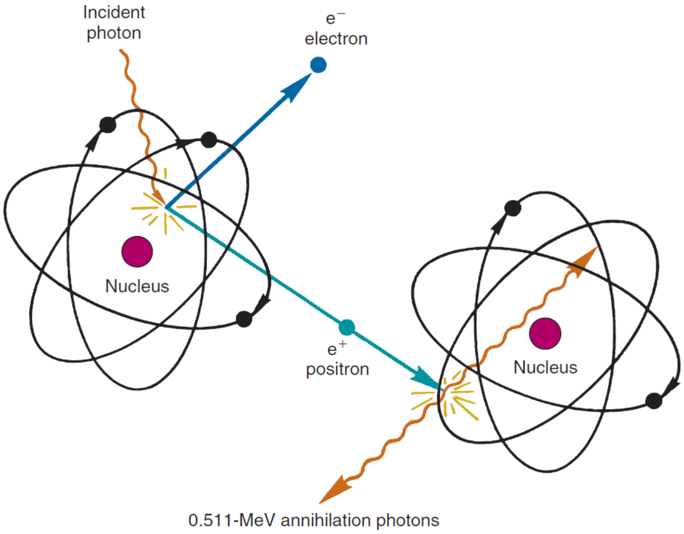

Figure 2.5 – A photon undergoing pair production in the Coulomb field of an atomic nucleus. The subsequent positron interaction is not part of the pair production interaction. Adapted from [27].

the photon energy.

2.2.4 Pair and triplet production

Pair production occurs when a photon decays into an electron and positron pair in the Coulomb field of the atomic nucleus. This is seen in Figure 2.5. Triplet production is similar except it occurs near an orbital electron and this third electron may be ejected. Pair production is the dominant interaction for high-energy photons. This interaction will not be considered in this thesis because the photon energies dealt with are below this interaction's threshold energy.

2.3 Photon interaction coefficients

For a given photon, the total atomic cross section σ is the sum of all the individual atomic interaction cross sections, i.e.,

$$\sigma = \sigma_{PE} + \sigma_R + \sigma_C + \sigma_{PP} + \sigma_{TP}. \tag{2.7}$$

In Equation 2.7, PE stands for photoelectric effect, C for Compton, R for Rayleigh, PP for pair production and TP for triplet production.

The macroscopic equivalent of the total atomic cross section is the mass-linear attenuation coefficient, $\frac{\mu}{\rho}$. It is given by

$$\frac{\mu}{\rho} = \frac{N_A}{A}\left[\sigma_{PE} + \sigma_R + \sigma_C + \sigma_{PP} + \sigma_{TP}\right] = \frac{\mu_{PE}}{\rho} + \frac{\mu_C}{\rho} + \frac{\mu_R}{\rho} + \frac{\mu_{PP}}{\rho} + \frac{\mu_{TP}}{\rho}, \tag{2.8}$$

where ρ is the element's physical density, N_A is Avogradro's number and A is the molar mass of the element. It is often given in cm^2/g. The mass-linear attenuation coefficient describes how "strongly" photons of a given energy interact with a medium.

2.3.1 Photon energy transfer coefficients

Photons, upon interacting, transfer some of their energy into the kinetic energy of charged particles. Energy transfer occurs during the photoelectric effect, Compton scattering and pair and triplet production. No energy is transferred during a Rayleigh interaction. For a photon interaction i, the interaction energy transfer fraction, $\bar{f}_{tr,i}$, is the fraction of initial photon energy transferred into the kinetic energy of charged particles. The mass-energy transfer coefficient, $\frac{\mu_{tr}}{\rho}$, is defined as

$$\frac{\mu_{tr}}{\rho} = \frac{\mu_{PE}}{\rho}\bar{f}_{tr,PE} + \frac{\mu_{C}}{\rho}\bar{f}_{tr,C} + \frac{\mu_{PP}}{\rho}\bar{f}_{tr,PP} + \frac{\mu_{TP}}{\rho}\bar{f}_{tr,TP} \tag{2.9}$$

$$= \frac{\mu_{tr,PE}}{\rho} + \frac{\mu_{tr,C}}{\rho} + \frac{\mu_{tr,PP}}{\rho} + \frac{\mu_{tr,TP}}{\rho}. \tag{2.10}$$

2.3.2 Photon energy absorption coefficients

Photon interactions that transfer energy to charged particles ultimately lead to dose deposition (see Section 1.2). Any charged particle kinetic energy that is converted into radiative losses (see Section 2.4) does not contribute to local dose deposition. The quantity that describes the amount of photon energy that ends up as deposited dose is the mass-energy absorption coefficient, $\frac{\mu_{en}}{\rho}$. This quantity is determined by the relation

$$\frac{\mu_{en}}{\rho} = \frac{\mu_{tr}}{\rho}(1-\bar{g}), \tag{2.11}$$

where $\bar{g}$ is the mean fraction of charged particle kinetic energy that is expended into radiative losses (bremsstrahlung, positron in-flight annihilation and fluorescence from electron impact ionization). The behaviours of the mass-linear attenuation and absorption coefficients can be seen in Figure 2.6.

2.4 Charged particle interactions

As a charged particle travels through a medium, it interacts with the medium's atomic constituents and loses kinetic energy. The rate at which charged particles lose kinetic energy

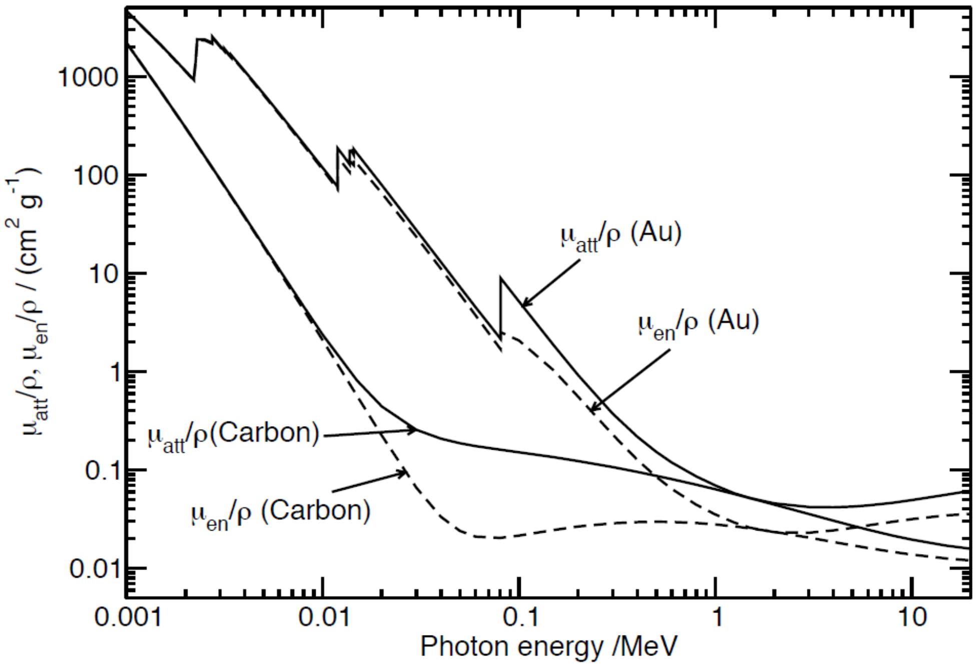

Figure 2.6 – The mass-linear attenuation and absorption coefficients for carbon and gold (Au). Note how at low photon energies, where the photoelectric effect is dominant, almost all photon energy is deposited. The K, L and M absorption edges of gold can be seen at low photon energies. Adapted from [36].

is described by the mass stopping power, $\frac{S}{\rho}$. It is usually expressed in units of $MeV \cdot cm^2/g$. The mathematical definition is

$$\frac{S}{\rho} = -\frac{1}{\rho}\frac{dE_K}{dx}, \tag{2.12}$$

where dE_K is the charged particle's kinetic energy loss and dx is the distance travelled. The charged particle may interact with a nucleus or orbital electrons in several ways. Inelastic collisions involve the incident charged particle interacting inelastically with orbital electrons and ejecting them from their orbitals. These ejected electrons (often called delta rays) go on to interact in a similar manner. This is the manner in which ionizing radiation causes energy to be deposited in a medium. The kinetic energy lost by the incident charged particle in this type of interaction is described by the mass-electronic stopping power, $\frac{S_{el}}{\rho}$. An incident charged particle may also undergo an inelastic radiative interaction, whereby it is accelerated by the Coulomb field of the nucleus or orbital electrons and radiates its kinetic energy away in the form of photons. This emitted radiation is known as *bremsstrahlung*. Radiative charged particle interactions of this type occur much more frequently with the nucleus than the orbital electrons. The energy lost through radiative interactions is given by the mass-radiative stopping power, $\frac{S_{rad}}{\rho}$. The stopping power can be written as a sum of these components

$$\frac{S}{\rho} = \frac{S_{el}}{\rho} + \frac{S_{rad}}{\rho}. \tag{2.13}$$

The total stopping power is a function of the electron kinetic energy. At low electron kinetic energies, the electronic stopping power energy dependence goes like $E^{-1} \ln E$, where E is the electron kinetic energy. At higher kinetic energies, beyond about 1 MeV, the electronic stopping power increases with kinetic energy, though less drastically. The radiative stopping power, for low electron kinetic energies and atomic numbers, is also much smaller than the electronic stopping power. This is why the assumption that $g \approx 0$ for kilovoltage photon beams is appropriate. Beyond a kinetic energy of 1 MeV, the radiative stopping power increases and eventually surpasses the electronic stopping power.

Other interactions that involve an incident charged particle losing energy are impact ionization and nuclear collisions. For electrons, the cross sections for these interactions are much smaller than the cross sections for the interactions mentioned in the paragraph above. Their stopping powers are therefore not included in Equation 2.13.

2.5 The production of medical radiation

Radiation for medical purposes is produced by specialized machines. For kilovoltage beam radiation therapy, x-rays are produced by an x-ray tube. A diagram illustrating the basic components of an x-ray tube are shown in Figure 2.7. The x-rays are produced from electrons that originate from a heated cathode. This cathode is a filament usually made of tungsten. As current runs through the filament, it is heated up and electrons are ejected through thermionic emission. The large potential difference (tube voltage) between the negative cathode and positive anode allows the electrons to flow to the positive end. For radiotherapy, this potential ranges from 40 to 300 kV, hence the name kilovoltage beam. The electrons are accelerated by this potential causing them to gain kinetic energy. Once the electrons reach the anode, they strike a target, usually made of tungsten. Upon striking the target, the electrons interact with the atoms and produce bremsstrahlung, as described in Section 2.4. Characteristic x-rays from the target are also produced if the incident electrons ionize any atoms. The bremsstrahlung x-rays then exit the tube perpendicularly to the electron flow. Before reaching the patient or water phantom, the x-ray beam passes through filters (copper, aluminum and tin combinations) and is collimated to the desired field size. The filters remove very low energy photons which deposit large entrance skin doses in the patient. The advantage of combining different material filters is that one filter can remove the fluorescence of another filter.

The electrons striking the target do not all have the same energy resulting in a spectrum of photon energies. This is why a kV beam is referred to by its tube potential and not a specific energy. The anode angle, target and filter materials and voltage waveform all affect the shape of this spectrum. Due to relaxation processes in the target and filters, K and L shell fluorescence are also present in the spectra. Some spectra used in the present work can be seen in Section 4.3.1.

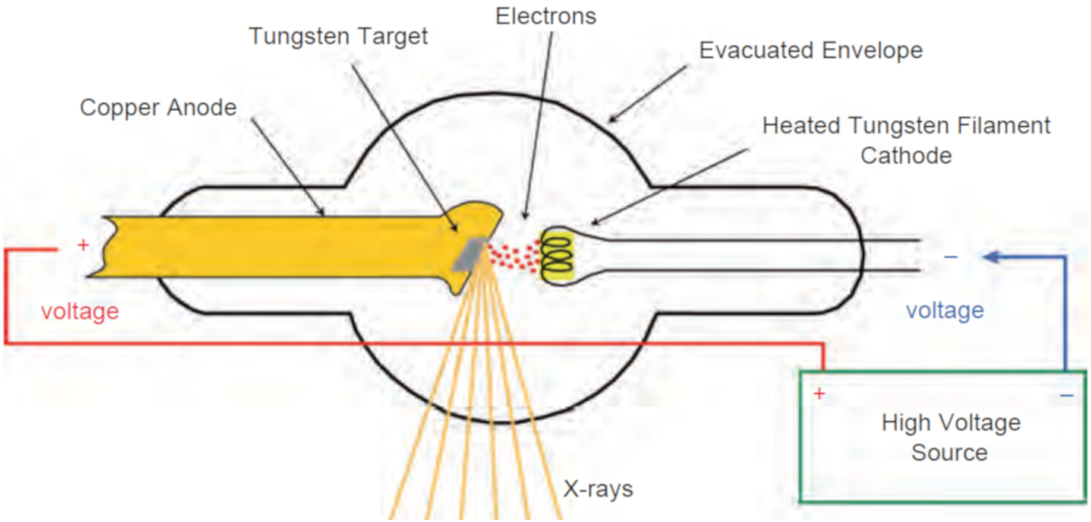

Figure 2.7 – A diagram of an x-ray tube and it's components. The electrons are accelerated by a potential difference and produce bremsstrahlung x-rays by striking a target. Adapted from [37].

X-ray tubes have limited potential to produce photon beams for radiotherapy because the photons never exceed an energy of 400 keV (some x-ray tubes exceed a tube potential of 300 kV). These photons will not be able to reach deep-seated tumours because of the large attenuation coefficients and the dose at such depths will be minimal due to the photon attenuation. These issues were overcome by the 1950's and 1960's with the introduction of medical linear accelerators (linac). Though the dosimetry of linacs is not discussed in this thesis, their radiation-generating operating principles are discussed here due to their ubiquity in the radiation therapy field. A schematic of one can be seen in Figure 2.8.

Similar to an x-ray tube, electrons are emitted through thermionic emission from a heated filament (cathode) and accelerated towards an anode. This occurs within the electron gun component. Since the cathode is always "on" (-20 kV), a grid with a potential less than that of the filament is used to keep the electrons from escaping the gun. At this point, no beam is produced. To produce a beam, the grid is switched to a positive potential through a voltage pulse from the pulsed modulator. The pulsed modulator is kept in sync with the pulses generated by the radio frequency (RF) power source. The RF power source generates

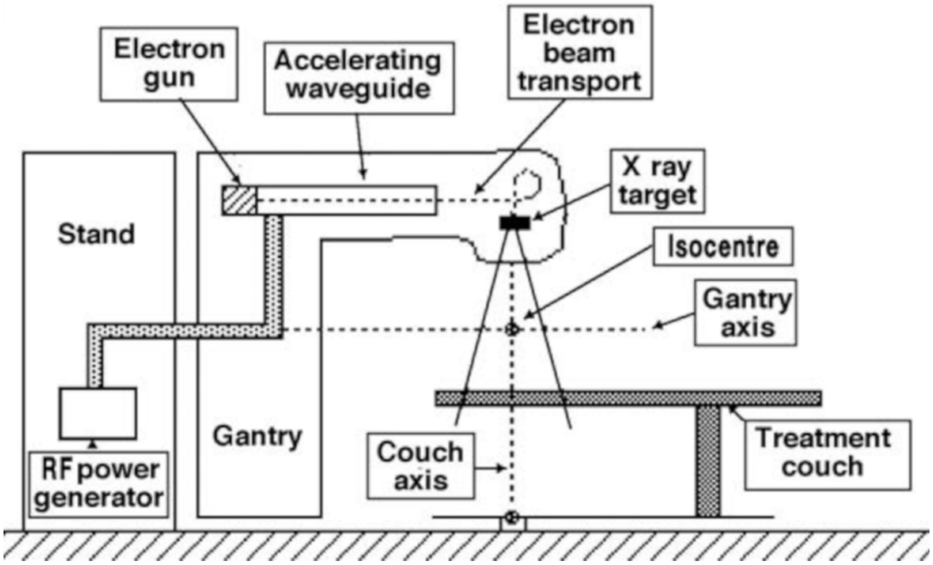

Figure 2.8 – Components of a medical linear accelerator. Adapted from [26].

electromagnetic waves that travel under vacuum to a waveguide. The waveguide is used to accelerate the electrons even further. The RF power source and accelerating waveguide combination is what ultimately leads to a linac producing higher energy photon beams than an x-ray tube. Focusing coils wrap around the waveguide to keep the electrons from deviating from a straight path. The electron beam is then bent by a magnet system so that it impinges perpendicularly on an x-ray target. Again, similar to an x-ray tube, the electrons interact within the target and bremsstrahlung is produced. The x-ray target may also be removed so that an electron beam is produced. Components within the linac head flatten the beam and also collimate it to the desired field size.

A clear distinction between x-ray tubes and medical linacs is the angle between the accelerated electron beam incident on the bremsstrahlung target and the emitted bremsstrahlung (photon beam) itself. For x-ray tubes, which produce kV photon beams, the angle between the electrons and the photon beam is 90°. For linacs (MV beams), the angle is 0°. The reason behind this distinction is the angular distribution of bremsstrahlung emission at different electron energies. In the case of x-ray tubes, where the electrons are in the keV range, bremsstrahlung is emitted at an angle of 90° or less relative to the electron direction of travel. In the case of linacs, where the electrons are in the MeV range, bremsstrahlung is emitted nearly parallel to the electron direction of travel. The yield of bremsstrahlung is also much greater for Mv beams in comparison to kV beams. This is due to the larger radiative stopping power for high energy electrons (see Section 2.4).

References

7. Report 85. *Journal of the International Commission on Radiation Units and Measurements* **11(1),** NP (2011).

18. Seltzer, S. M. *et al.* ICRU Report 90. Key data for ionizing-radiation dosimetry: Measurement standards and applications. *Journal of the International Commission on Radiation Units and Measurements* **14(1)** (2016).

25. *Scattering Cross Section Physics* `<ahref="https://www.pngkit.com/view/u2e6t4w7q8r5q8a9_500px-scatteringdiagram-svg-scattering-cross-section-physics/"target="_blank">500px-scatteringdiagramSvg-ScatteringCrossSectionPhysics@pngkit.com</a>`. Accessed: 11/07/2019.

26. Podgorsak, E. B. *Radiation Oncology Physics: A Handbook for Teachers and Students* (IAEA, Vienna, Austria, 2005).

27. Cherry, S. R., Sorenson, J. A. & Phelps, M. E. *Physics in Nuclear Medicine* 4th ed. (Elsevier, Philadelphia, PA, USA, 2012).

28. Fano, U., McVoy, K. W. & Albers, J. R. Sauter Theory of the Photoelectric Effect. *Phys. Rev.* **116(5),** 1147–1156 (1959).

29. Scofield, J. H. *Theoretical photoionization cross sections from 1 to 1500 keV.* tech. rep. (1973). doi:10.2172/4545040.

30. Sabbatucci, L. & Salvat, F. Theory and calculation of the atomic photoeffect. *Radiation Physics and Chemistry* **121,** 122–140 (2016).

31. Saloman, E. B. & Hubbell, J. H. *X-Ray Attenuation Coefficients (Total Cross Sections): Comparison of the Experimental Data Base With the Recommended Values of Henke and the Theoretical Values of Scofield for Energies Between 0.1-100 keV* (National Bureau of Standards, Gaithersburg, MD, USA, 1986).

32. Saloman, E. B., Hubbell, J. . & Scofield, J. H. X-ray attenuation cross sections for energies 100 eV to 100 keV and elements Z = 1 to Z = 92. *Atomic Data and Nuclear Data Tables* **38(1),** 1–196 (1988).

33. Büermann, L. *et al.* Measurement of the x-ray mass energy-absorption coefficient of air using 3 keV to 10 keV synchrotron radiation. *Physics in Medicine and Biology* **51(20),** 5125–5150 (2006).

34. Klein, O. & Nishina, Y. Über die Streuung von Strahlung durch freie Elektronen nach der neuen relativistischen Quantendynamik von Dirac. *Zeitschrift für Physik* **52(11),** 853–868 (1929).

35. Ribberfors, R. Relationship of the relativistic Compton cross section to the momentum distribution of bound electron states. *Phys. Rev. B* **12,** 2067–2074 (1975).

36. Andreo, P., Burns, D. T., Nahum, A. E., Seuntjens, J. & Attix, F. H. *Fundamentals of Ionizing Radiation Dosimetry* 2nd ed. (Wiley, 2017).

37. Bushberg, J. T., Seibert, J. A., Leidholdt Jr, E. M. & Boone, J. M. *The Essential Physics of Medical Imaging* 3rd ed. (Lippincott Williams & Wilkins, Philadelphia, PA, USA, 2011).

Chapter 3

Radiation Dosimetry

3.1 Dosimetric quantities and concepts

In the previous chapter, individual photon and electron interactions were discussed. They explain how ionizing radiation causes energy/dose to be transferred to a medium. Radiation dosimetry aims to quantify and measure (or determine) absorbed dose or related dosimetric quantities. These dosimetric quantities are non-stochastic, i.e., are averages of large numbers of interactions. The dosimetric quantities that are crucial to the work of this thesis are discussed in this chapter.

3.1.1 Fluence

Fluence is a radiometric quantity that quantifies the amount of particles (charged or uncharged) crossing a point. Denoted as Φ, the fluence is defined to be the quotient of dN by da, where dN is the number of particles incident on a sphere of cross-sectional area da about a given point [7]. Mathematically,

$$\Phi = \frac{dN}{da}. \tag{3.1}$$

Since the radiation beam is made up of particles of different energies moving in particular directions, it makes more sense to talk about the fluence spectrum Φ_E (also simply called the spectrum). The fluence spectrum, differential in energy, is written as

$$\Phi_E = \frac{d\Phi}{dE}. \tag{3.2}$$

Summing this fluence spectrum over all energies E present in the spectrum recovers the fluence, i.e.,

$$\Phi = \int_0^{E_{max}} \Phi_E \; dE. \tag{3.3}$$

Analogous definitions to the fluence and fluence spectrum can be made for the total amount of energy crossing a point. The energy fluence spectrum (energy spectrum), Ψ_E, differential in energy, is defined as

$$\Psi_E = E\Phi_E \;, \tag{3.4}$$

for any given particle energy E. The energy fluence, Ψ, is recovered through the following relation

$$\Psi = \int_0^{E_{max}} \Psi_E \; dE. \tag{3.5}$$

3.1.2 Kerma

Uncharged particles, such as photons and neutrons, can transfer some of their energy to charged particles as kinetic energy (for photons see Chapter 2). The kinetic energy released per unit mass or Kerma is defined to be the mean sum of the initial kinetic energies of all the charged particles, dE_{tr}, liberated in a mass dm of a material by uncharged particles incident on dm [18]. This mean sum also includes the kinetic energy of any electrons released from atomic relaxation processes (Auger electrons). The mathematical definition for kerma (K) is

$$K = \frac{dE_{tr}}{dm}. \tag{3.6}$$

For a photon fluence spectrum, Φ_E, the kerma K is calculated with the following equation

$$K = \int_0^{E_{max}} E\Phi_E \frac{\mu_{tr}(E)}{\rho} dE = \int_0^{E_{max}} \Psi_E \frac{\mu_{tr}(E)}{\rho} dE. \tag{3.7}$$

A related quantity is the electronic (or collisional) kerma, K_{el}. Electronic kerma excludes the radiative losses of liberated charged particles. Thus,

$$K_{el} = K(1-\bar{g}) = \int_0^{E_{max}} E\Phi_E \frac{\mu_{tr}(E)}{\rho}(1-g(E))dE = \int_0^{E_{max}} \Psi_E \frac{\mu_{en}(E)}{\rho} dE \tag{3.8}$$

where $\bar{g}$ is the mean radiative fraction and $g(E)$ is the radiative fraction for photons of energy E (or more accurately the charged particles a photon of energy E creates). Note how from Equation 3.8, a mean energy fluence weighted mass-energy absorption coefficient can be defined to be

$$\frac{\overline{\mu_{en}}}{\rho} = \frac{\int_0^{E_{max}} \Psi_E \frac{\mu_{en}(E)}{\rho} dE}{\int_0^{E_{max}} \Psi_E \ dE} = \frac{K_{col}}{\Psi} \tag{3.9}$$

One can see through Equation 3.8 that if electron radiative losses are negligible ($g \approx 0$), kerma is approximately equal to electronic kerma.

Under the condition known as charged particle equilibrium (CPE), the electronic kerma is equal to the absorbed dose, i.e.,

$$D \overset{CPE}{=} K_{el}. \tag{3.10}$$

CPE exists when the number of charged particles of a given type, energy and direction entering a region is equal to those exiting a region. The energy carried away by an exiting charged particle is replaced by the dose deposited by an entering charged particle. This total dose is equal to the exiting charged particle's electronic kerma. Any radiative interaction occurring inside the region also occurs outside of it. This is how the equality between electronic kerma and absorbed dose can be understood. In practice, CPE is never truly exists. This is because the photons of the radiation beam are attenuated over the range of the secondary electrons produced up-stream. As such, the energy deposited by electrons (dose) at one point in a medium is greater than the electronic kerma at the same point. At these points in a medium, which are typically past the maximum range of the secondary electrons, the absorbed dose is proportional to the electronic kerma. This type of equilibrium is known as transient charged particle equilibrium (TCPE). Under TCPE, the dose-electronic kerma relation can be written as

$$D \overset{TCPE}{=} \beta K_{el}, \tag{3.11}$$

where β is a constant of proportionality greater than unity. Note how CPE is a special case of TCPE with $\beta = 1$ (negligible photon attenuation over the maximum secondary electron range).

3.1.3 Percent depth dose

A percentage depth dose (PDD) is a relation between the depth in a medium and the absorbed dose to the medium at that depth on the central axis of the radiation beam. The absorbed dose at a given depth is given as a percentage of the maximum dose. Examples of photon PDDs can be seen in Figure 3.1. Percentage depth doses depend on the radiation type, energy, field size and the distance of the surface of the medium from the source (source-to-surface distance, SSD). Photon PDDs are characterized by a buildup region prior to the depth of maximum dose (the depth where 100% of the maximum dose is deposited). This occurs because photons travel some distance through the medium before interacting. The lack of photon interactions results in a low-electron fluence which is gradually built-up as photons are attenuated. For kV photons, the attenuation coefficient is large enough and the electron ranges short enough so that the depth of maximum dose is essentially at the surface of the medium. Past the depth of maximum dose, the dose decreases with depth due to attenuation decreasing the amount of photons. It can be seen in Figure 3.1 that the PDD for kV photons decreases much quicker than MV photons. This is due to the much larger attenuation coefficient at low photon energies.

3.2 Cavity theory

The main goal of reference radiation dosimetry is to determine the absorbed dose to an undisturbed medium at a reference point, D_{med}. This medium is typically water. A radiation dosimeter can only measure the absorbed dose to the medium of it's respective sensitive volume, D_{det}. In this section the dosimeter may be also called the detector. For the case of an air-filled ionization chamber, the sensitive volume medium is dry air. To obtain the absorbed dose to the undisturbed medium, one must be able to determine a factor that

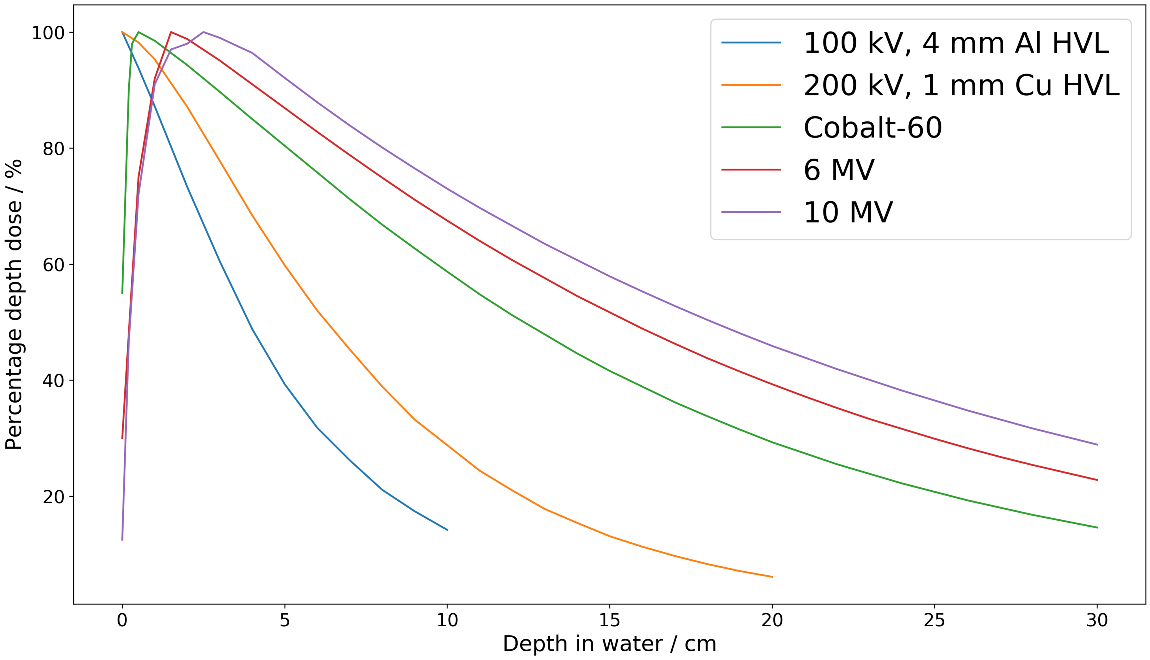

Figure 3.1 – Percentage depth doses of various photon beams. The source-to-surface distance for all beams is 100 cm except for the 200 kV beam (SSD = 50 cm) and the 100 kV beam (SSD = 30 cm). The field size for all beams is 10x10 cm^2 except for the 100 kV beam (circular field size = 10 cm diameter). Data from BJR Supplement 25 [38] and Khan [39].

converts from the dose to detector to the dose to the medium. This is the purpose of Cavity theory. The word "cavity" is used because the detector acts as a cavity within the surrounding medium. In general, it is difficult to establish an analytical relationship between the dose to the detector and the dose to the medium. Monte Carlo simulations play an enormous role in this context. In this section, two analytical methods are discussed. These methods are approximations in that they can only be used under certain conditions. In Section 4.4, cavity theory will be used to analyze the uncertainty on the calculated chamber correction factors.

Before discussing these methods, a relationship between absorbed dose and stopping power is introduced for charged particles. The derivation is not given here but is given in the textbook by Andreo *et. al.* [36]. For a spectrum of charged particles, under the condition of δ-CPE (CPE for delta rays) or total CPE, the absorbed dose to a medium, D_{med}, is related to the medium's mass-electronic stopping power, $(S_{el}/\rho)_{med}$, through the expression

$$D_{med} = \int_0^{E_{max}} \Phi_{med,E} \left(\frac{S_{el}(E)}{\rho} \right)_{med} dE, \tag{3.12}$$

where $\Phi_{med,E}$ is the charged particle fluence spectrum.

3.2.1 Bragg-Gray cavity theory

Consider a radiation detector or "cavity", placed in a medium at a reference point, with a sensitive volume made of a low-density material, such as air. If a megavoltage photon beam is made to be incident upon the medium, the energetic secondary electrons produced by the photons will have ranges large enough so that they will be able to traverse the entire cavity and the electron fluence is left undisturbed. There will also be a negligible amount of photon interactions within the cavity producing secondary electrons. These conditions are often called the *Bragg-Gray conditions*. It is in this sense that the cavity is considered to be "small" for electrons. Note how the energy of the electrons and the material of the cavity are relevant to the cavity being small, not just it's physical dimensions. Due to these conditions, the electron fluence crossing the cavity is essentially the same as that in the undisturbed medium at the same point. A cavity acting in this manner is known as a *Bragg-Gray cavity*. Using Equation 3.12, the ratio of the dose in the undisturbed medium to that in the detector, D_{med}/D_{det}, can be written as

$$\frac{D_{med}}{D_{det}} = \frac{\int_0^{E_{max}} \Phi^{e,prim}_{med,E} \left(\frac{S_{el}(E)}{\rho} \right)_{med} dE}{\int_0^{E_{max}} \Phi^{e,prim}_{med,E} \left(\frac{S_{el}(E)}{\rho} \right)_{det} dE}, \tag{3.13}$$

where $\Phi^{e,prim}_{E,med}$ is the "primary" electron fluence (as in just the secondary electrons liberated by primary photons) in the medium. These fluences are used because the energy deposited by all subsequent delta rays are already included in the stopping powers. The medium and detector electronic mass-stopping powers are denoted as $(S_{el}(E)/\rho)_{med}$ and $(S_{el}(E)/\rho)_{det}$, respectively. Thus, in the case of small cavities, the medium-to-detector stopping power ratio is the conversion factor from dose to detector to dose to medium.

3.2.2 Spencer-Attix cavity theory

In practice, delta ray equilibrium does not often exist. This is because high energy delta rays produced in the cavity by electronic collisions are not balanced by incoming, similar energy delta rays. In these cases, Bragg-Gray cavity theory is not applicable. Spencer-Attix cavity theory [40] takes into account these high energy delta rays by considering two energy regimes. The energy cut-off between the two regimes is denoted as Δ. The energy cut-off Δ is chosen to be the energy sufficient enough for an electron to just traverse the entire cavity. For ionization chamber cavities made of air, Δ is between 10 and 15 keV. Delta rays with energies below Δ are assumed to deposit their energy locally. Delta rays with energies above Δ are added to the total electron fluence spectrum. The total electron fluence spectrum contains all generations of electrons. According to the Bragg-Gray conditions, the total electron fluence spectrum in the cavity is equal to that in the undisturbed medium. According to Spencer-Attix cavity theory, the ratio D_{med}/D_{det} can be written as

$$\frac{D_{med}}{D_{det}} = \frac{\int_{\Delta}^{E_{max}} \Phi_{med,E}^{e,tot} \left(\frac{L_{\Delta}(E)}{\rho}\right)_{med} dE + TE_{med}}{\int_{\Delta}^{E_{max}} \Phi_{med,E}^{e,tot} \left(\frac{L_{\Delta}(E)}{\rho}\right)_{det} dE + TE_{det}}, \tag{3.14}$$

where $\Phi_{E,med}^{e,tot}$ is the total electron fluence in the medium. The medium and detector restricted electronic mass-stopping powers are denoted as $(L_{\Delta}(E)/\rho)_{med}$ and $(L_{\Delta}(E)/\rho)_{det}$, respectively. Restricted electronic stopping powers only consider electron collisions that result in an energy transfer of Δ or less. The track end terms in the medium and the detector, TE_{med} and TE_{det}, take into account the energy deposition by electrons with initial kinetic energies of Δ or below. They are written as

$$TE_{med} = \Phi^{e,tot}_{E,med}(\Delta) \left(\frac{S_{el}(\Delta)}{\rho} \right)_{med} \Delta \tag{3.15}$$

and

$$TE_{det} = \Phi^{e,tot}_{E,med}(\Delta) \left(\frac{S_{el}(\Delta)}{\rho} \right)_{det} \Delta \tag{3.16}$$

3.2.3 Large cavities

When the incident photon energies are low, as is the case for kilovoltage x-ray beams, one can no longer use Bragg-Gray cavity theory. Secondary electrons originating from the surrounding medium, the wall of the detector or the detector cavity itself may stop within the detector cavity due to their small ranges. Photon interactions also occur more frequently within the cavity. It is in this sense the detector is considered "large" for electrons. For kV photons in general, electron ranges are short and therefore there is a practical equivalence of absorbed dose and electronic kerma. Using Equations 3.8, 3.9 and 3.11, the ratio D_{med}/D_{det} is therefore

$$\frac{D_{med}}{D_{det}} \overset{TCPE}{=} \frac{\beta_{med}\ K_{col,med}}{\beta_{med}\ K_{col,det}} = \frac{\beta_{med}\ \int_0^{E_{max}} \Psi_{med,E} \left(\frac{\mu_{en}(E)}{\rho} \right)_{med} dE}{\beta_{det} \int_0^{E_{max}} \Psi_{det,E} \left(\frac{\mu_{en}(E)}{\rho} \right)_{det} dE} = \frac{\beta_{med}\ \Psi_{med}\ (\overline{\mu_{en}}/\rho)_{med}}{\beta_{det}\ \Psi_{det}\ (\overline{\mu_{en}}/\rho)_{det}}\ . \tag{3.17}$$

Here, two assumptions can be made. First, the ratio $\beta_{med}/\beta_{det} \approx 1$ and second, the photon energy fluence crossing the cavity is equal to that in the undisturbed medium at the same point i.e., $\Psi_{med} \approx \Psi_{det}$. This implies the cavity is small in relation to the photon mean free paths. The dose ratio can then be simplified to

$$\frac{D_{med}}{D_{det}} = \frac{(\overline{\mu_{en}}/\rho)_{med}}{(\overline{\mu_{en}}/\rho)_{det}} \ , \tag{3.18}$$

which is simply the ratio of the medium-to-detector mean energy fluence weighted mass-energy absorption coefficients.

3.3 Ionization chambers

Ionization chambers are the most common dosimeter in radiation dosimetry. In general, an ionization chamber consists of a chamber wall and an (dry) air cavity containing a central electrode [41]. A schematic of a generic Farmer-type cylindrical ionization chamber can be seen in Figure 3.2. The Farmer design is the most common design for clinically-used ionization chambers [42]. The air cavity is kept at a constant pressure and has a nominal volume of 0.6 g/cm^3. The air cavity is considered the sensitive volume of the detector. The chamber wall is solid and the material is usually graphite, Polymethyl methacrylate (PMMA) or an air or water-equivalent plastic. The wall is typically made thick enough to establish CPE. The thickness of the chamber wall is on the order of a few tenths of a millimeter. The wall also acts as an outer electrode. The central electrode takes the shape of a cylinder, is typically 1 mm is diameter and is typically made of aluminium. An insulator is wrapped around the central electrode at the base of the air cavity and beyond to ensure the collected charge does not leak from the central electrode. A guard electrode is wrapped around the insulator to ensure the uniformity of the electric field and re-directs any leakage current away from the central electrode. The stem of the chamber can be considered as the sum of the

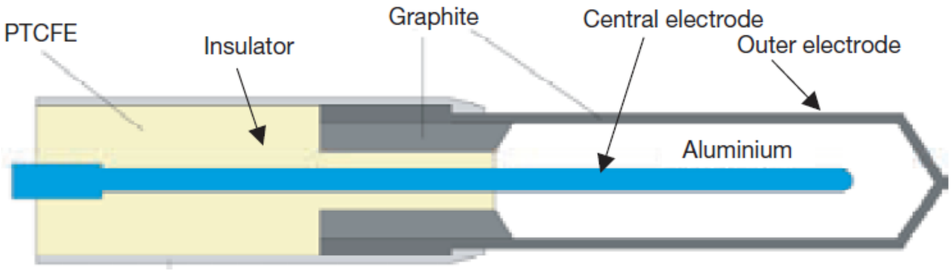

Figure 3.2 – Schematic for a generic Farmer-type cylindrical ionization chamber. Adapted from [26].

components past the air cavity.

An ionization chamber operates on the basis of charge collection. For photon beams, the incident photons interact within the medium surrounding the chamber, the chamber wall and the air cavity. The secondary electrons which travel to the air cavity go on to ionize the air molecules. The charge released from these ionization events are collected by the central electrode. A potential difference between the outer and central electrode (usually +300 V) causes the charges to travel to the central electrode. The reading of an ionization chamber measurement is the collected charge, typically given in nanocoulombs (nC) with a precision in the range of sub pC. The charge is read by an electrometer. It can now be seen why calibration coefficients are required to obtain kerma or absorbed dose for clinical ionization chamber dosimetry.

Ionization chambers apart from the Farmer chamber do exist and see uses in specialized scenarios. Parallel-plate chambers are used in electron beams [43] and very low energy photon beams [44]. Well-type chambers can be used for the dosimetry of brachytherapy sources.

3.3.1 Ionization chamber characteristics

There are certain inherent characteristics of an ionization chamber, or any dosimeter for that matter, that are important to consider for radiation dosimetry. While some of these characteristics are desirable, others are not and require special consideration. These characteristics can often be discussed in the context of the detector response, M/F, where M is the detector reading and F is a dosimetric quantity such as absorbed dose to water, absorbed dose to the detector's sensitive volume or air kerma.

Linearity

The reading of a detector should be linearly proportional to the absorbed dose to it's sensitive volume (air cavity in the case of an ionization chamber). In other words, response is constant for a reading of any magnitude for a given radiation beam quality. Of course, non-linear behaviour may occur outside a certain dose range. Usage of the detector outside of this dose range should be limited and any readings corrected if taken in this range.

Dose rate dependence

As an ionization chamber measures a time-integrated signal, the reading should not depend on the dose rate of the radiation field. The response should be independent of dose rate. In practice, there is only a limited range in where a detector is dose rate independent.

Directional dependence

The geometrical orientation of the detector in relation to the incident radiation field may have an effect upon the reading or response of the detector. In the case of cylindrically symmetric ionization chambers, such as Farmer-type chambers, directional dependence comes from construction design or imperfections. The directional dependence is often completely negligible for ionization chambers (except in magnetic fields). For other dosimeters that are not symmetric, their orientation is important. During routine use, detectors should be used in the same orientation as the orientation used during their calibration.

Energy dependence

The response M/F of a detector depends on the energy or beam quality of the incident radiation beam. This is the energy dependence of the detector. Ideally, the response is independent of beam quality but this does not occur in practice. In practice, a detector must be calibrated at every beam quality the user has available. This typically occurs for the air kerma calibration coefficient, N_K, for kilovoltage beam dosimetry. If only one beam quality is used to calibrate a detector, as is typically the case in megavoltage beam dosimetry with Cobalt-60, the calibration coefficient requires a beam quality dependent correction factor. The energy dependence of a detector's air kerma or absorbed dose to water response can be due to differences in stopping power or mass energy-absorption coefficient ratios at different beam qualities. If the dose-to-the-detector response D_{det}/M has an energy dependence this is known as "intrinsic energy dependence". Intrinsic energy dependence is associated with the fundamental relation between the reading of the detector M and the dose to the detector D_{det} being energy dependent. For example, for an ionization chamber, $D_{\mathrm{det}}/M = \frac{W_{\mathrm{air}}}{e}\frac{1}{m_{\mathrm{air}}}$, which, due to the energy dependence of W_{air}, becomes non-constant for photon energies of below about 10 keV. Intrinsic energy dependencies also require correction (or are managed by calibration).

3.3.2 Ionization chamber measurements

Ionization chambers are calibrated at a PSDL under reference conditions. If a raw ionization chamber reading, M_{raw}, is not taken under reference conditions in the clinic, then it must corrected to the value it would be under reference conditions.

Pressure and temperature

Among other parameters, reference conditions specify the ambient temperature and pressure, which are taken to be the SATP values (298.15 K/22°C and 101.3 kPa). For reference dosimetry to be done, ionization chamber readings must be given at SATP. As is often the case, a raw ionization chamber reading is taken at a non-SATP temperature and pressure. The reading must be corrected to SATP temperature and pressure through a correction factor P_{TP}.

Charge collection efficiency

In theory, all of the charge produced in the chamber cavity by an incident radiation beam should be collected by the ionization chamber. In reality, an ionization chamber never has a collection efficiency of 100% [45]. The effects that reduce the chamber collection efficiency are *initial recombination* and *general recombination*. Initial recombination occurs when positive and negative charge carriers that originate from the same charged particle track recombine [46]. This includes the recombination of an electron and its parent ion. Initial recombination is more likely for densely-ionizing radiation such as protons and heavy ions than electron or photon beams. This type of recombination is dose rate-independent because it concerns a single charged particle track and is independent of the track density within the ionization chamber cavity. Initial recombination depends on the potential difference applied to the chamber, the specific type of chamber and the incident radiation type and energy. General (or volume) recombination occurs when positive and negative charge carries from different charged particle tracks recombine. This type of recombination is dose rate-dependent because it depends on the track density within the chamber cavity. General recombination is also dependent on whether the radiation beam is pulsed or continuous. This is due to differences in the charge carrier diffusion time scale.

An ionization chamber reading must be corrected for these ion recombination effects. The ion recombination correction factor is denoted as P_{ion}. This correction factor should be less than 1% for a nominal Farmer ionization chamber.

Polarity

The magnitude of the charge collected by an ionization chamber might change if the polarity of the potential difference is reversed. This is due to charge being created by Compton interactions in the central electrode (Compton current) and charge being created in the non-cavity regions of the chamber such as the stem and the cable connecting the chamber to the electrometer (extracameral current). This polarity effect is corrected for with a polarity correction factor, P_{pol}.

To summarize, the corrected ionization chamber reading M is written as

$$M = M_{raw} P_{TP} P_{ion} P_{pol}. \tag{3.19}$$

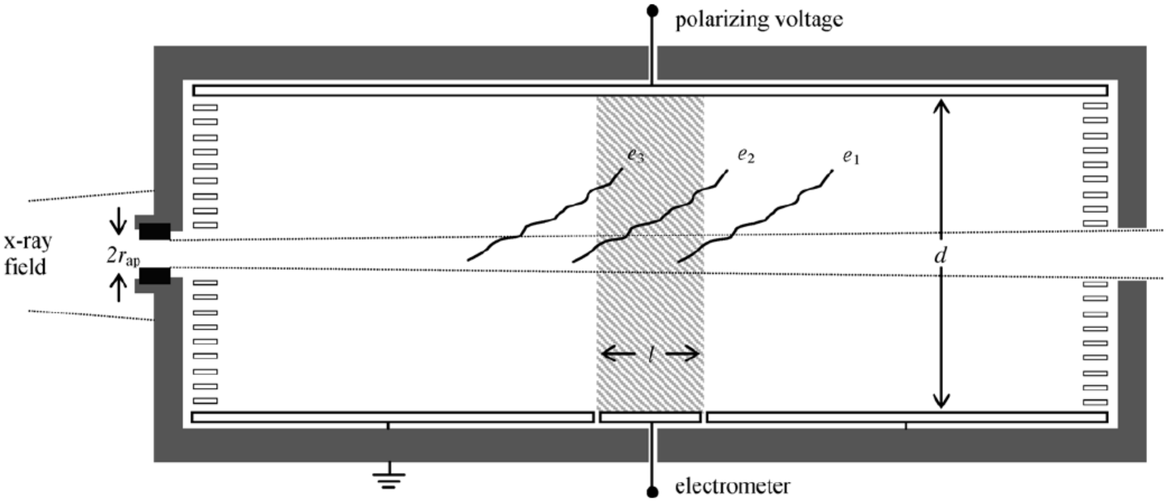

Figure 3.3 – Diagram of a free air chamber. The aperture is defined by the radius r_{ap}. The collecting electrode is defined by the length l. The collecting volume for charge is defined by l and d (shaded region). The photons interact within the air to produce electrons e_1, e_2 and e_3. The existence of CPE within the collecting volume allows the collected charge to be equated to the charge liberated by photons in the sub-region created by the intersection of the collecting volume and the radiation field. Adapted from [47].

3.4 Radiation primary standards

Ionization chambers for clinical reference dosimetry must be calibrated against a radiation primary standard. Recall that a primary standard measures a quantity of interest directly with extremely high accuracy and is independent of instruments that measure the same quantity [36]. In this section, air kerma and calorimetery-based absorbed dose to water primary standards will be discussed.

3.4.1 Free air chambers

The free air chamber, an example of which is shown in Figure 3.3, is an air kerma primary standard for photons with energies below 300 keV. The photon beam first passes through the aperture of the chamber. As the photons travel through air, they transfer kinetic energy to secondary electrons. A pair of parallel-plate electrodes, separated by a distance d, establishes a potential difference. The liberated electrons are collected by a collecting electrode of length l connected to an electrometer. The length of the collecting electrode and the electrode separation distance defines the collecting volume (shaded area in Figure 3.3). Even though the radiation field interacts within a sub-region of the collecting volume (intersection of radiation field with shaded region in Figure 3.3), the existence of CPE allows the liberated charge within this sub-region to be equated to the total charge collected, even if some of the collected charge does not originate from within this sub-region. Air kerma of primary photons (at the position of the aperture) is then given by

$$K_{air} = \frac{q}{m_{air}} \left(\frac{W_{air}}{e} \right) \frac{1}{(1 - \bar{g}_{air})} \prod_i k_i, \tag{3.20}$$

where q is the collected charge, m_{air} is the mass of air of the sub-region created by the intersection of the collecting volume and the radiation field, (W_{air} is the mean energy expended by an electron to produce an ion pair in dry air (33.97 eV), e is the unit electron charge and the k_i are correction factors. Because W_{air} is known only for dry air, a correction factor corrects for any humidity present in the air. Any kerma due to non-primary photons, such as scattered photons and fluorescence, is not desired and dealt with through correction factors. Photon attenuation through air, electron loss, ion recombination, polarity effects, electric field distortions and photon transmission through the walls defining the aperture are also corrected for [47].

3.4.2 Calorimetry

Calorimetry is based on the principle that energy deposition in a medium by ionizing radiation causes the medium's temperature to rise [48]. By measuring this temperature rise, the absorbed dose to the medium can be determined. This makes water calorimetry the most absolute method of measuring the absorbed dose to water. The relation between the induced temperature rise in the medium m, ΔT_m, and absorbed dose to water, D_w, is

$$D_w = c_{m,p}\ \Delta T_m\ f_{w,m} \prod_i k_i, \tag{3.21}$$

where $c_{m,p}$ is the specific heat capacity at constant pressure of the medium, $f_{w,m}$ is a conversion factor between the absorbed dose to water under reference conditions in water and the absorbed dose to the medium during calorimeter irradiation conditions. The k_i's are correction factors. For water calorimetry, $f_{w,w}$ is unity. Conductive and convective heat transfer affect the measured temperature rise. To obtain the true temperature rise caused by energy absorption, the heat transfer is corrected for through a correction factor, or procedures are carried out during analysis of the calorimetric temperature trace to account for heat loss. Other correction factors also correct for the radial non-uniformity of the radiation beam at the measurement point, the presence of non-water materials in the beam path and any radiation-induced chemical reactions (heat defect). Water calorimetry experiments are often performed at 4°C (277.15 K) instead of 298.15 K (SATP conditions). This causes the density of water to be different than that at SATP. The effects of this change in water density is corrected for in a "temperature" or "density" correction factor. The temperature rise during absorbed dose calorimetry is small, on the order of milliKelvins (mK). The temperature rise is often measured with thermistors, resistors whose resistance is temperature-dependent. See [48, 49] for a more in-depth discussion of the technical implementation of thermistors in water calorimetry. As an example of a water calorimeter, the one used at Germany's national metrological institute, the Physikalisch-Technische Bundesanstalt (PTB), and the measurement results in kV beams of which are used for comparison in this thesis, is shown in Figure 3.4.

Water calorimeters have been used for high-accuracy dosimetry in MV beams [50–52] and

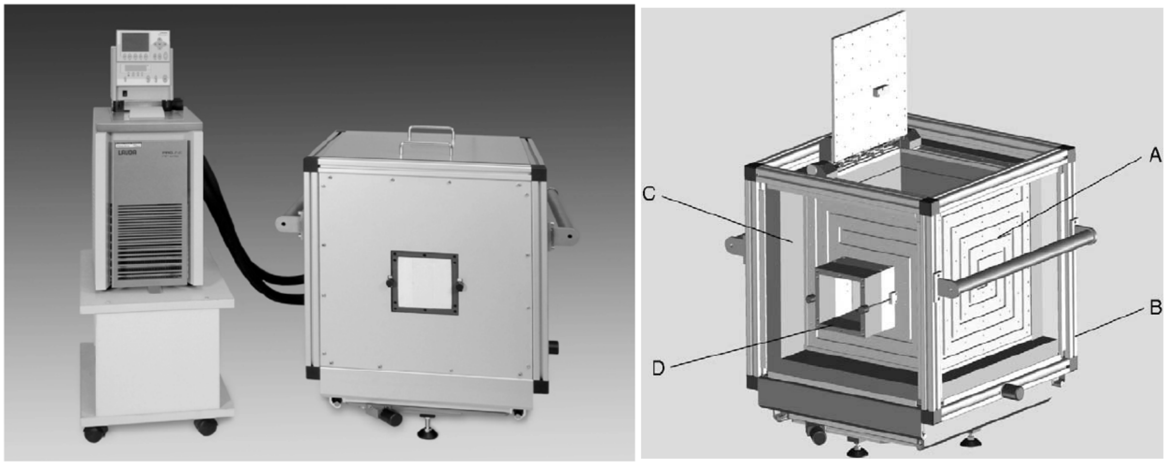

(a) (b)

Figure 3.4 – The Physikalisch-Technische Bundesanstalt (PTB) water calorimeter. Adapted from [53].

kV beams (see Section 1.5). A general concern with kV beams is the lower dose rates that limit the precision of absorbed dose to water calorimetry measurements. In addition, due to the long irradiation times needed to establish a sufficient signal for kV beams, significant heat loss occurs and the heat loss correction factor introduces a significant uncertainty in the overall absorbed dose to water determination.

3.5 Radiation beam quality

It is important to specify or characterize a given radiation beam so that reference dosimetry comparisons between two beams are meaningful. A radiation beam can be fully characterized by determining the energy and angular distribution of all types of particles at all points in a phantom. It is very difficult to establish these quantities and a simpler approach to characterize a radiation beam is required. A simpler approach is to use a parameter or a set of parameters that define the *quality* of a radiation beam so that quantities of dosimetric interest, such as calibration coefficients or stopping power ratios, can be described to an acceptable accuracy. These parameters are known as *beam quality specifiers*. A radiation

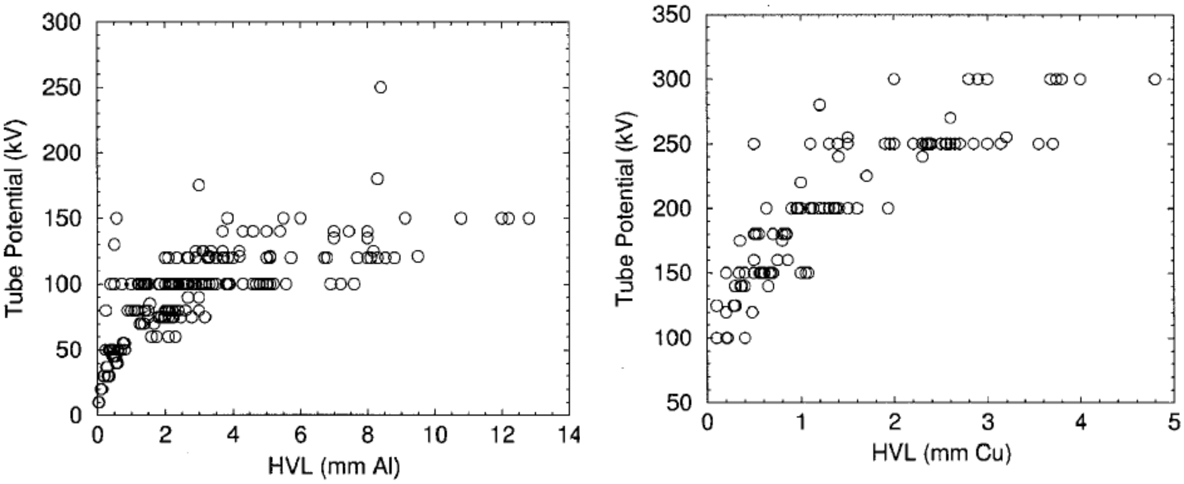

(a) (b)

Figure 3.5 – A variety of kV x-ray beams of varying tube potential and half value layer. These figures show how one parameter does not completely specify an x-ray beam. Adapted from [9].

beam quality is often denoted by Q. Measuring and obtaining the fluence spectrum of a radiation beam is another method of characterization but these measurements are too involved for routine purposes.

Kilovoltage beams have two beam quality specifiers, the tube potential (kV) and the half value layer (HVL). The HVL, given in mm Al or mm Cu, is the thickness of material required to reduce the x-ray fluence by one half. Two specifiers are required because various x-ray beams of the same kV can have different HVLs, as seen in Figure 3.5. This is because the photon fluence spectra produced by x-ray tubes of a given potential (or a given HVL) are not all the same and are also determined by the amount of beam filtration used.

For megavoltage (MV) photon beams, the photon component of the PDD at 10 cm depth in a water phantom, $PDD(10)_x$, is used in TG-51 as the beam quality specifier. Using just the accelerating potential is not sufficient for the same reasons given above. Just the photon component is specified because there is electron contamination within a megavoltage photon beam which contributes to the total PDD. The measured $PDD(10)_x$ values are corrected for electron contamination. For MeV electrons, the beam quality specifier is the depth in a water phantom expressed in cm at which the PDD reaches 50%, R_{50}.

References

7. Report 85. *Journal of the International Commission on Radiation Units and Measurements* **11(1),** NP (2011).

9. Ma, C.-M. *et al.* AAPM protocol for 40–300 kV x-ray beam dosimetry in radiotherapy and radiobiology. *Medical Physics* **28(6),** 868–893 (2001).

18. Seltzer, S. M. *et al.* ICRU Report 90. Key data for ionizing-radiation dosimetry: Measurement standards and applications. *Journal of the International Commission on Radiation Units and Measurements* **14(1)** (2016).

26. Podgorsak, E. B. *Radiation Oncology Physics: A Handbook for Teachers and Students* (IAEA, Vienna, Austria, 2005).

36. Andreo, P., Burns, D. T., Nahum, A. E., Seuntjens, J. & Attix, F. H. *Fundamentals of Ionizing Radiation Dosimetry* 2nd ed. (Wiley, 2017).

38. Aird, E. G. A. *et al. Central axis depth dose data for use in radiotherapy. Brit. J. Radiol. Suppl 25.* (The British Institute of Radiology, London, UK, 1996).

39. Khan, F. M. & Gibbons, J. P. *Khan's The Physics of Radiation Therapy* 5th ed. (Wolters Kluwer, 2014).

40. Spencer, L. V. & Attix, F. H. A Theory of Cavity Ionization. *Radiation Research* **3(3),** 239–254 (1955).

41. Boag, J. W. in *The Dosimetry of Ionizing Radiation* (eds Kase, K. R., Bjärngard, B. E. & Attix, F. H.) 169–243 (Academic Press, 1987).

42. Aird, E. G. A. & Farmer, F. T. The design of a thimble chamber for the Farmer dosemeter. *Physics in Medicine and Biology* **17(2),** 169–174 (1972).

43. Almond, P. R. *et al.* AAPM's TG-51 protocol for clinical reference dosimetry of high-energy photon and electron beams. *Medical Physics* **26(9),** 1847–1870 (1999).

44. Podgorsak, E. B., Gosselin, M. & Evans, M. D. C. Superficial and orthovoltage x-ray beam dosimetry. *Medical Physics* **25(7),** 1206–1211 (1998).

45. Boag, J. W. & Currant, J. Current collection and ionic recombination in small cylindrical ionization chambers exposed to pulsed radiation. *The British Journal of Radiology* **53(629),** 471–478 (1980).

46. Christensen, J. B., Tölli, H. & Bassler, N. A general algorithm for calculation of recombination losses in ionization chambers exposed to ion beams. *Medical Physics* **43(10),** 5484–5492 (2016).

47. Burns, D. T. & Büermann, L. Free-air ionization chambers. *Metrologia* **46(2),** 9–23 (2009).

48. Seuntjens, J. & Duane, S. Photon absorbed dose standards. *Metrologia* **46(2),** 39–58 (2009).

49. Sarfehnia, A. *Water calorimetry-based radiation dosimetry in iridium-192 brachytherapy and proton therapy.* PhD diss. (McGill University, QC, 2010).

50. Palmans, H., Mondelaers, W. & Thierens, H. Absorbed dose beam quality correction factors for the NE2571 chamber in a 5 MV and a 10 MV photon beam. *Physics in Medicine and Biology* **44(3),** 647–663 (1999).

51. McEwen, M. R. Measurement of ionization chamber absorbed dose factors in megavoltage photon beams. *Medical Physics* **37(5),** 2179–2193 (2010).

52. De Prez, L., de Pooter, J., Jansen, B. & Aalbers, T. A water calorimeter for on-site absorbed dose to water calibrations in ^{60}Co and MV-photon beams including MRI incorporated treatment equipment. *Physics in Medicine and Biology* **61(13),** 5051–5076 (2016).

53. Krauss, A. Heat conduction effects during the calorimetric determination of absorbed dose to water in radiotherapy beams. *Thermochimica Acta* **445(2),** 126–132 (2006).

Chapter 4

Monte Carlo Simulations

4.1 The Monte Carlo method

Monte Carlo (MC) or the *Monte Carlo method* has been used to simulate the process of radiation transport in matter. In this section, a brief overview of what constitutes a radiation transport Monte Carlo code is given. The radiation transport toolkit used in this thesis, EGSnrc, is introduced.

Monte Carlo relies on random number sampling and probability distributions. At the microscopic level, radiation transport is probabilistic. Particle path lengths, interaction probabilities and scattering angle and energy deposition are all based on probability distributions which are derived from mathematical models of these processes [54]. For medical physics purposes, Monte Carlo is used to determine deterministic dosimetric quantities such as absorbed dose in complex geometries. As the result of a simulation is an average, an associated type A (statistical) uncertainty on the mean is also given. Because the scored quantities are Poisson distributed, convergence of the average to the true mean can be achieved by increasing the number of simulated particles. Reducing the type A uncertainty, σ_{A}, can be achieved by increasing the number of simulated particles, following the rule $\sigma_{\mathrm{A}} \sim 1/\sqrt{N}$.

4.2 The EGSnrc toolkit

The EGSnrc (Electron-Gamma-Shower nrc) radiation transport toolkit is a set of computer codes developed at the National Research Council of Canada (NRCC) [55]. EGSnrc is used for the Monte Carlo simulations of photon and electron transport in arbitrary geometries. Photons and electrons can be transported down to kinetic energies of 0.001 MeV. All photon and electron processes discussed in Chapter 2 and more are taken into account. The user is able to define their own geometries. Custom materials can also be defined by the user with the PEGS4 code. Several different beam sources and geometries can be defined. Several photon interaction cross section databases are also available to the user.

4.2.1 The `egs_chamber` user code

The EGSnrc user code `egs_chamber` is a C++ based code that is able to model arbitrary geometries and beam sources and score dose [56]. This user code is used primarily to model detectors in phantoms. Ionization chambers will be modeled in this thesis. Absorbed dose can be scored in user-selected regions of the entire geometry. Various techniques known as *variance reduction techniques* (VRTs) have been implemented in `egs_chamber`. Variance reduction techniques are meant to improve simulation efficiency while introducing no systematic error [57]. The simulation efficiency is quantified by the parameter ϵ which is equal to $1/\sigma_A^2 T$, where T is the total amount of CPU time. The VRTs used in this thesis, Russian roulette, photon cross section enhancement (XCSE) and range rejection are discussed below.

4.2.2 Variance reduction techniques

Particle weight

The particle weight is introduced to all particles in a simulation to keep track of the variance reduction techniques applied to them. If a technique is applied to a particle, its weight is modified.

Russian roulette

Russian roulette is a rejection routine that is applied to electrons and photons. In a game of Russian Roulette, it is determined whether a particle survives or not by generating a random number and comparing it to a user-defined survival probability $1/N_r$. Of course,

$N_r \geq 1$. If the random number is less than the survival probability, the particle survives and continues being transported with its weight scaled by N_r (the weight is divided by survival probability). If the particle does not survive (the random number is greater than the survival probability), it is discarded. This technique aids in reducing the number of electrons that need to be transported during the simulation.

Photon cross section enhancement (XCSE)

In a region of the geometry with XCSE turned on, the total photon cross section is scaled (enhanced) by a whole number factor $b > 1$. In the regions with XCSE turned on, b times more secondary electrons are produced. The increased number of electrons reduce the type A uncertainty of the final result and reduce the number of initial particles. Biasing is avoided in the following manner. In the region with XCSE turned on, the incident photon is split into an interacting portion with a fraction of $1/b$ and a non-interacting portion with a fraction of $1 - 1/b$. The non-interacting portion does not have its direction or energy changed by the interaction. All electrons set in motion and scattered photons will have a weight of w_0/b, w_0 being the weight of the incident photon. Any scattered photons and relaxation photons or bremsstrahlung that follow this interaction will undergo a Russian roulette game with a survival probability of $1/b$. The non-interacting portion of the incident photon also undergoes a Russian roulette game with a survival probability of $1 - 1/b$. In the end, all photons have a weight of w_0.

Range rejection

Range rejection is variance reduction technique that discards electrons based on their range and distance from a user-defined cavity. Russian roulette is often used in conjunction with this technique. Electrons who cannot reach a user-defined cavity and are outside this cavity undergo a game of Russian Roulette. Whether the electron can reach the cavity or not is determined by calculating its range in the medium and comparing it to the smallest distance to the cavity. If the range is less then this smallest distance, a game of Russian Roulette is played. If an electron is in the cavity and cannot escape, it is discarded if its total energy is less than a user-defined energy, E_{save}.

4.3 Ionization chamber correction factor simulations

In order to calculate the ionization chamber correction factors, all of the components of Equation 1.5 must be calculated individually. In order to extract the product of the overall chamber correction factor $P_{Q,cham}$ and the waterproof sheath correction factor P_{sheath}, Equation 1.5 must be re-written as

$$P_{Q,cham}P_{sheath} = \frac{\left(\frac{D_{w,z=2cm}}{K_a}\right)\left(\frac{M_a}{M_w}\right)}{\left[\left(\frac{\mu_{en}}{\rho}\right)_{w,a}\right]_{w,Q,z=2cm}} \; . \tag{4.1}$$

In Equation 4.1, the air kerma calibration coefficient, N_K, has been expanded as the ratio of the air kerma free in air, K_a, and the corrected ionization chamber reading reading with the chamber free in air, M_a. (Equation 1.2). For all but one ionization chamber used in this thesis, the NE2571 chamber, $P_{sheath} = 1$. In this section, the simulation setup of each component of Equation 4.1 will be discussed. The simulation parameters for all simulations are summarized in Table 4.1. Simulation specific parameters are given in the respective following sections.

Item name	Description	References
Code, version/release date	EGSnrc (v2018), `egs_chamber`, `flurznrc` and `g` user codes, `egs++` geometry package	[55, 56]
Validation		[58]
Timing	123 cores, Intel(R) Xeon(R) CPU E5-2687W 0 @ 3.10GHz, 20 to 200 total CPU hours	
Source description	Collimated point source with measured photon fluence spectrum. A 9.85 cm diameter field size is defined at the reference point (2 cm depth in the water phantom) 100 cm away from the source.	[59]
Cross-sections	Renormalized xcom photon cross sections. NIST ESTAR density effect corrections and mean excitation energies with ICRU 90 values for liquid water, dry air and graphite. NRC bremsstrahlung cross sections.	[18, 30, 60]
Transport parameters	ECUT & AE = 0.512 MeV PCUT & AP = 0.001 MeV Photon cross section = mcdf-xcom Spin effects = On Bound Compton scattering = On Rayleigh scattering = On Atomic Relaxations = On Brems cross sections = NRC EXACT boundary crossing algorithm PRESTA-II electron-step algorithm All other parameters set to default	[55]
Variance reduction techniques	Absorbed dose to water simulations XCSE factor = 1024 Ionization chamber simulations XCSE factor = 512 Russian roulette survival probability = 1/1024 E_{save} = 0.512 MeV	[55, 57]
Scored quantities	Absorbed dose to a water disk (0.8 cm diameter, 0.025 cm thickness) at a depth of 2 cm in a water phantom (30x30x30 cm^3) on the central beam axis 100 cm away from the source. Absorbed dose to ionization chamber air cavity at 2 cm depth in a water phantom or free-in-air, 100 cm away from the source. The midpoint of the cavity is centered on the central beam axis. For the ionization chambers simulated, see Table 4.3. Photon fluence spectra at a depth of 2 cm in a water phantom in a water disk (0.1 cm in height and 1 cm^2 in area), 100 cm away from the source on the central beam axis. Water and air mass energy-absorption coefficients averaged over the in-phantom photon energy spectrum. Air kerma.	
# histories/statistical uncertainty	400×10^6 to 40×10^9 histories Under 0.03% statistical uncertainty for all simulations except the in-phantom ionization chamber simulations, which were under 0.07% statistical uncertainty.	
Statistical methods	History-by-history	
Postprocessing	See Equation 4.1	[8–11]

Table 4.1 – Monte Carlo simulation parameters for the simulations carried out in this thesis, presented here according to the recommendations of TG-268 [61].

kV	Filtration (mm Al)	Filtration (mm Cu)	Mean photon energy (keV)	HVL (mm Cu)
50	4.0		31.6	0.073
70	4.0		42.2	0.108
100	4.5		52.4	0.192
120	6.0		59.5	0.303
140	9.0		67.1	0.477
150	4.0	0.5	78.0	0.836
200	4.0	1.0	99.6	1.581
250	4.0	1.6	123.4	2.498
280	4.0	3.0	147.7	3.38
300	4.0	3.0	152.3	3.592

Table 4.2 – Characteristics of the kilovoltage beams used in this thesis. The mean photon energy is the mean fluence spectrum weighted energy. This energy is defined in air at a distance of 100 cm away from the source. Obtained from PTB [59].

4.3.1 Radiation beam qualities

The radiation qualities (PTB radiation quality series TH) used in these simulations are the exact same as those used in the measurements performed by PTB. The fluence spectrum of each quality was measured at PTB with a high-purity Ge spectrometer 100 cm away in air from the x-ray source and were kindly supplied to us by the PTB. The tube voltages ranged from 50 kV to 300 kV. The kV x-ray facilities at the PTB are described in more detail by Krauss *et. al.* [22]. These measured fluence spectra were used in the definition of the beam sources in all simulations. The radiation quality characteristics are shown in Table 4.2. Some measured and *Spk*-calculated spectra can be seen in Figures 4.1 and 4.2, respectively. The calculated spectra are only used for the uncertainty analysis described below.

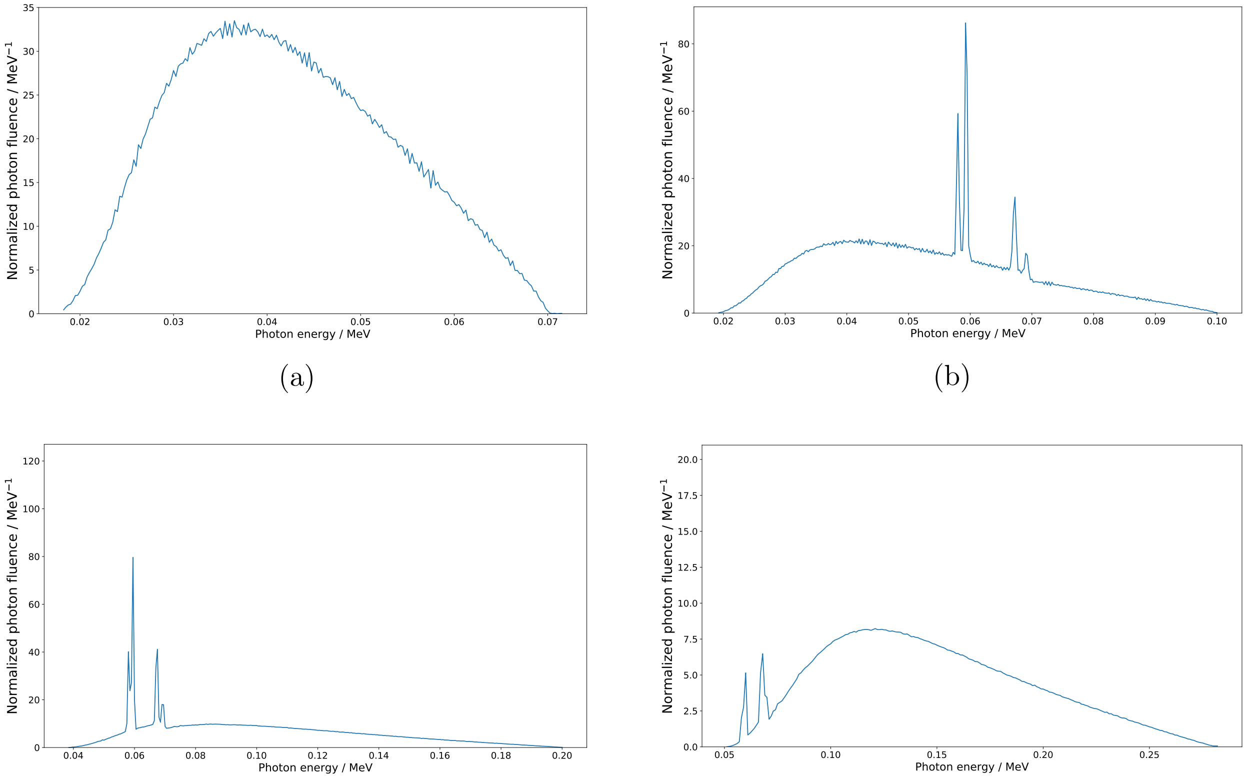

(a) (b)

(c) (d)

Figure 4.1 – Photon fluence spectra measured by PTB normalized by the total photon fluence. The tube voltages are 70 kV (a), 100 kV (b), 200 kV (c) and 280 kV (d).

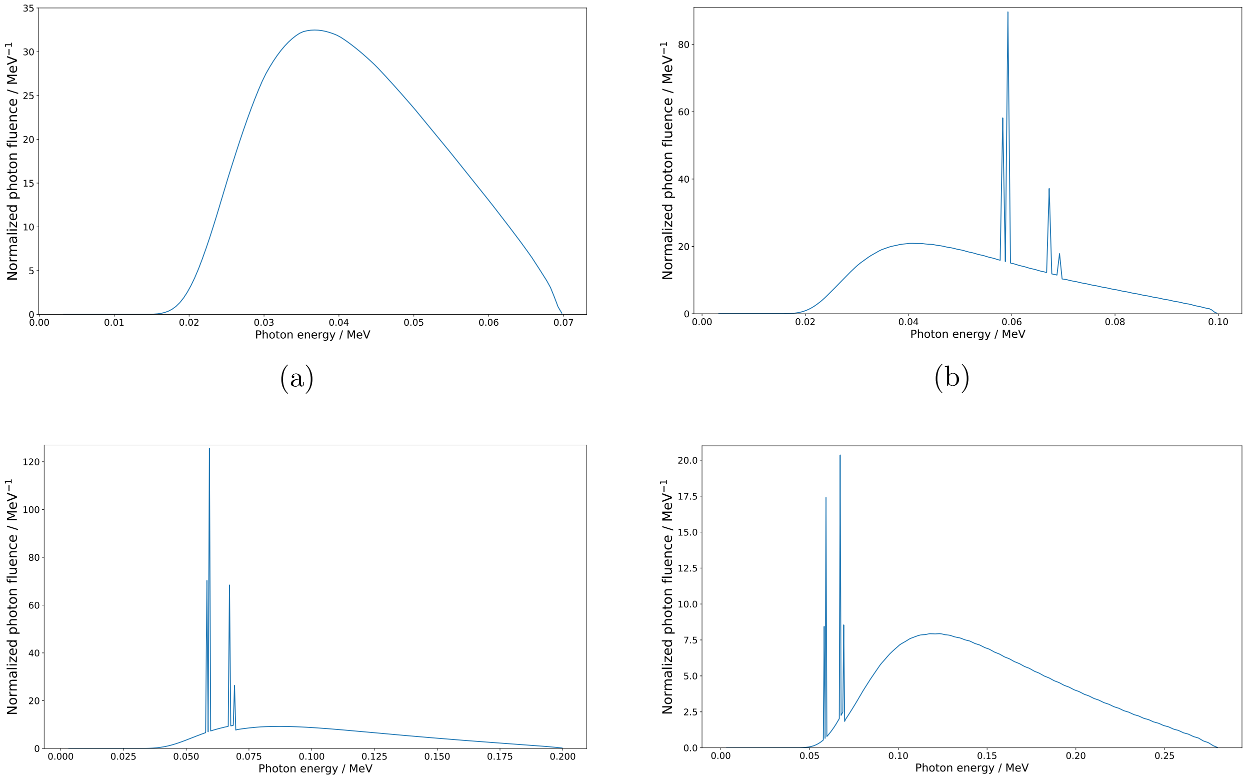

(a) (b)

(c) (d)

Figure 4.2 – Photon fluence spectra calculated with *Spk* [62], an updated version of the x-ray spectra calculation program *Spekcalc* [63]. The spectra are normalized by the total photon fluence. These spectra were calculated using the beam characteristics of Table 4.2 and take into account the anode material (W) and angle and the entrance window of the x-ray tube. These spectra are defined in air at a distance of 100 cm away from the source. The tube voltages are 70 kV (a), 100 kV (b), 200 kV (c) and 280 kV (d).

4.3.2 Absorbed dose to water at 2 cm simulations

The absorbed dose to water at a reference depth of 2 cm in a water phantom, $D_{w,z=2cm}$, was calculated with the EGSnrc (v2018) user code `egs_chamber`. The geometry of the absorbed dose to water simulations is shown in Figure 4.3. The water phantom is modelled as a 30x30x30 cm^3 box. The reference point is set to be 100 cm away from the beam source on the central beam axis (98 cm source-to-surface distance). The beam source is defined as a collimated point source with the photon spectra supplied by PTB. Since the spectra were measured in air, any air attenuation between the beam source and the phantom is already "contained" in the spectra. An approximation is also made here; that the measured in-air spectra defined at a distance of 100 cm away from the source is equivalent to the spectra at a distance of 98 cm away from the source. This approximation is reasonable because the linear attenuation coefficient of air is small and the differences in distance (2 cm) is small. In theory, the desired field size at the reference point is 10 cm in diameter. In reality and in the simulations, a beam diameter of 9.85 cm is defined at the reference point to account for the finite size of the beam focal spot [22]. A thin disk of water with a diameter of 0.8 cm and a thickness of 0.025 cm is used to approximate a point. The disk is centered at the reference point and at a depth of 2 cm. The absorbed dose to water is scored in the disk. The simulations were run in pegsless mode with NRC bremsstrahlung corrections. To run in pegsless mode, a density effect correction file is required. This file contained ICRU Report 90 based liquid water density effect corrections and mean excitation energy (78 eV). The electron and photon production cutoffs AE and AP were set to 0.512 MeV and 0.001 MeV, respectively. The electron and photon transport cutoffs ECUT and PCUT were set to 0.512 MeV and 0.001 MeV, respectively. This ensures that all electrons and photons down to kinetic energies of 0.001 MeV are transported. Renormalized photoelectric cross sections from Sabbatucci & Salvat [30] were used for these simulations (option `mcdf-xcom` for `photon cross sections`). Bound Compton scattering (RIA), Rayleigh scattering, atomic

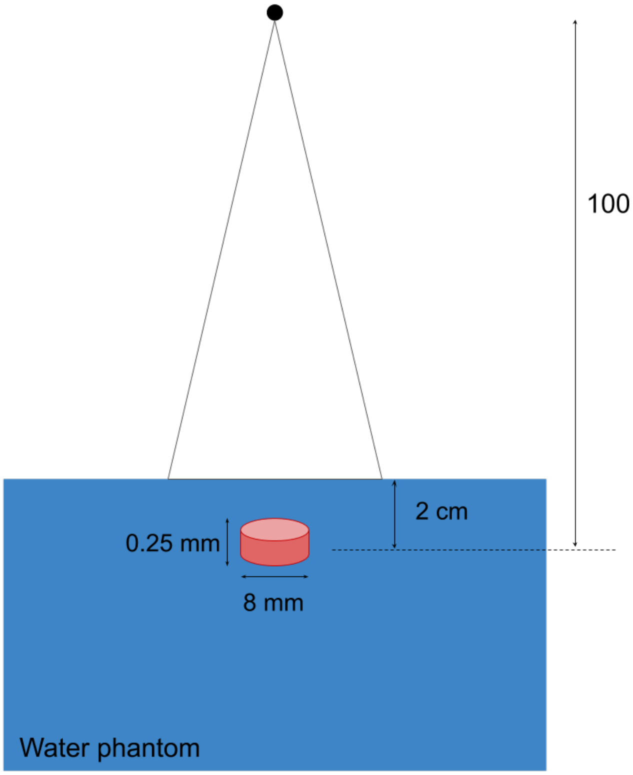

Figure 4.3 – The geometry of the absorbed dose to water simulations. The reference depth is 2 cm in a 30 x 30 x 30 cm^3 water phantom. The reference point is a distance of 100 cm away from the beam source. The red disk at the reference point is used to approximate the dose to a point. Its medium is also set to water. The beam diameter at the reference point is 9.85 cm. The black dot at the top represents the point beam source.

relaxations and spin effects were turned on. NRC bremsstrahlung cross sections were used. All other transport parameters were set to the EGSnrc defaults. The Russian roulette variance reduction technique was turned on with a survival probability of $1/1024$ and an E_{save} of 0.512 MeV. Photon cross section enhancement was used with an enhancement factor of 1024.

4.3.3 Ionization chamber simulations

The individual components of the chamber reading ratio M_a/M_w (Equation 4.1) cannot be determined through simulations directly because they are in units of charge and only dose can be scored with EGSnrc. A chamber reading M can be related to the dose to the chamber's air cavity, D_{cav}, through the well-known relation

$$D_{cav} = \frac{M}{m_{air}} \left(\frac{W_{air}}{e} \right) k_W k_{ii} \ , \tag{4.2}$$

where m_{air} is the mass of dry air in the cavity, W_{air} is the mean energy required to be expended by an electron to produce one ion pair in dry air (33.97 eV) and e is the unit electron charge. The correction factor k_W corrects for the increase in W_{air} at low photon energies. This is due to electron elastic and excitation interactions becoming more probable at low energies. This results in less ionization events and an increase in W_{air} [18]. The correction factor k_{ii} corrects for the inclusion of initial electrons in M. These electrons should not be included because the definition of W_{air} pertains only to the charge produced by such an electron slowing down in dry air. Both of these correction factors are photon energy-dependent. Using Equation 4.2, the ratio M_a/M_w can then be written as

$$\frac{M_a}{M_w} = \frac{m_{air} D_{cav,a} (W_{air}/e)}{m_{air} D_{cav,w} (W_{air}/e)} \frac{(k_W k_{ii})_w}{(k_W k_{ii})_a} = \frac{D_{cav,a}}{D_{cav,w}} \frac{(k_W k_{ii})_w}{(k_W k_{ii})_a} \ , \tag{4.3}$$

where $D_{cav,a}$ and $D_{cav,w}$ are the dose to the chamber cavity free-in-air and in water at a depth of 2 cm, respectively. The quantities $(k_W k_{ii})_a$ and $(k_W k_{ii})_w$ are the correction factors free-in-air and in water at a depth of 2 cm, respectively. At the photon energies comprising the x-ray spectra used in this work, this ratio is essentially unity for all radiation qualities. Therefore,

$$\frac{M_a}{M_w} \approx \frac{D_{cav,a}}{D_{cav,w}} \ . \tag{4.4}$$

In the ionization chamber simulations, the dose to the chamber cavity is scored.

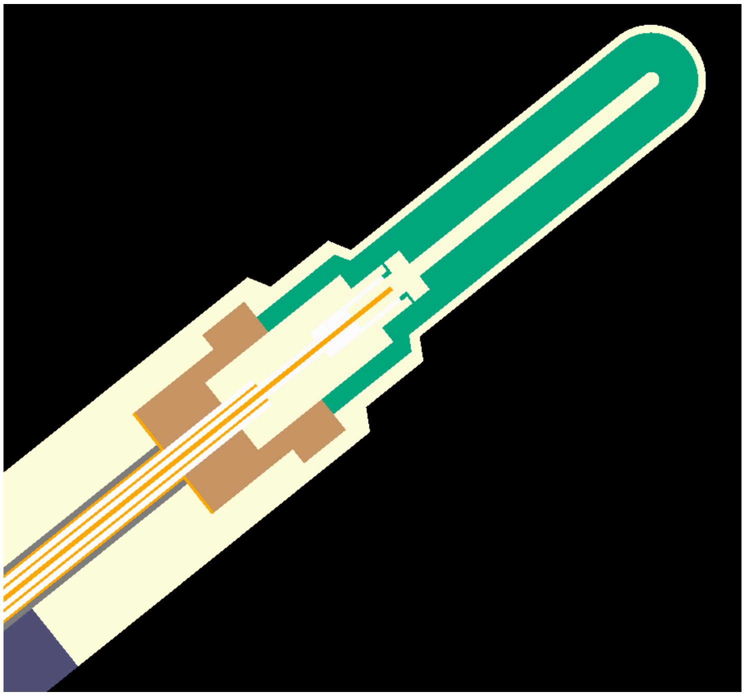

Figure 4.4 – A cross section of the Exradin A12 ionization chamber `egs_chamber` model. The surrounding water phantom is not shown.

Five Farmer-type ionization chambers are used in this work; the PTW TM30013, the NE2571, the IBA FC65-G and FC65-P and the Exradin A12. These chambers were modelled in `egs_chamber` and, except for the NE2571, are based on manufacturer-provided blueprints. An example of a chamber model for the Exradin A12 can be seen in Figure 4.4. The freely available user manual specifications for these ionization chambers are given in Table 4.3. Blueprint specifications are not given due to their proprietary nature. The geometry for the free-in-air and in-phantom simulations can be seen in Figure 4.5a and 4.5b, respectively. All of the ionization chambers modelled here are waterproof except the NE2571. For the in-phantom simulations with the NE2571, a 1 mm PMMA sheath was added to the model.

In each simulation, the centre of the chamber cavity was placed at the reference point. The dose was scored in the cavity of the chambers. The beam source, beam geometry, transport parameters and physics parameters were the same as those used in Section 4.3.2. For materials that were not supplied with EGSnrc, density effect correction files were generated with

	Wall		Electrode			Cavity			
Chamber	Material	Thickness (mm)	Material	Radius (mm)	Length (mm)	Volume (cm^3)	Radius (mm)	Length (mm)	Waterproof
PTW TM30013	PMMA/Gr	0.335/0.09	Al	0.575		0.6	3.05	23.0	Y
NE2571	Gr	0.36	Al	0.5	20.5	0.66	3.14	23.2	N
IBA FC65-G	Gr	0.4	Al	0.5	20.5	0.65	3.1	23.1	Y
IBA FC65-P	POM	0.4	Al	0.5	20.5	0.65	3.1	23.1	Y
Exradin A12	C552	0.5	C552	0.5	21.6	0.64	3.05		Y

Table 4.3 – Freely available user manual specifications of the ionization chambers used in this thesis. The materials are polymethyl methacrylate (PMMA), graphite (Gr), polyoxymethylene (POM), aluminum (Al) and air equivalent plastic (C552). Chambers that are not waterproof (NE2571) are modelled with a 1 mm PMMA sheath for the in-phantom simulations. Any information left out is due to it not being freely available.

data from the ESTAR database [60] and used in the simulations through pegsless mode. ICRU Report 90 data for the mean excitation energies and density effect corrections for graphite, dry air and liquid water were used in their respective density effect correction files (supplied by EGSnrc). The AE and AP parameters for all materials were set to 0.512 MeV and 0.001 MeV, respectively. A photon cross section enhancement factor of 512 was used for the in-air and in-phantom simulations. Russian roulette was turned on and the chamber cavity set as the rejection cavity. A survival probability of 1/1024 was used.

4.3.4 Air kerma and water-to-air mass-energy absorption coefficient ratio calculations

The air kerma, K_a, was calculated using the EGSnrc user code `g`. The only required inputs for these simulations were the photon spectra and the medium (air). All transport and physics parameters remained the same as in previous simulations.

The water-to-air mass-energy absorption coefficient ratio averaged over the photon energy fluence spectrum, $\left[(\overline{\mu_{en}}/\rho)_{w,a}\right]_{w,Q,z=2cm}$, is defined at the reference point in a water phantom at a depth of 2 cm. The calculation of this quantity first required the photon spectrum at

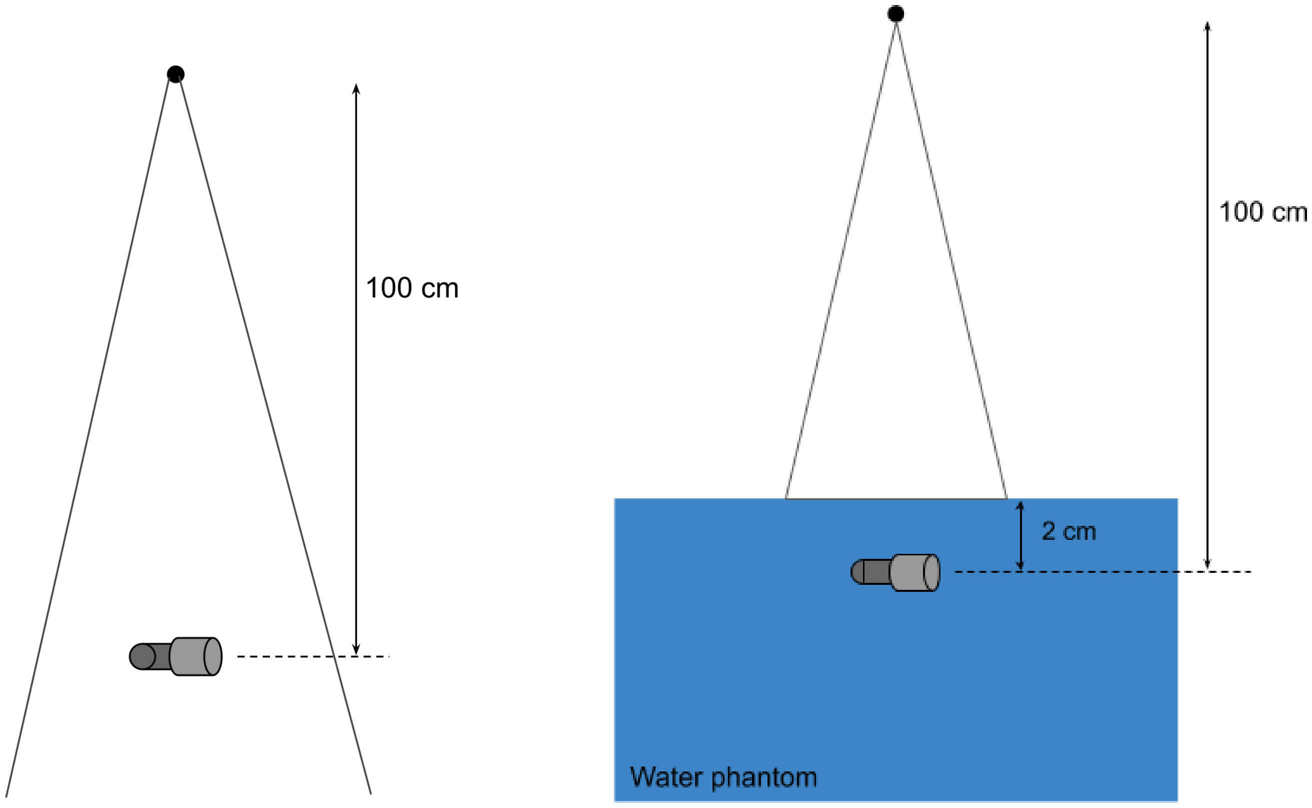

(a) (b)

Figure 4.5 – Geometries of the (a) free-in-air ionization chamber and (b) in-phantom ionization chamber simulations. The beam diameter is 9.85 cm at the reference point. The black dots at the top represent point beam sources.

2 cm in a water phantom at the reference point. These in-phantom spectra were calculated with the EGSnrc user code `flurznrc`. In these simulations, the in-air PTB x-ray spectra are transported to a depth of 2 cm in a water phantom. To approximate the reference point, these in-phantom spectra were calculated in a small water disk 0.1 cm in height and 1 cm^2 in area. Due to the restrictions of the user code, the water phantom was modelled as a cylindrical volume with a radius of 25 cm and a height of 30 cm. The beam source, beam geometry transport, transport parameters and physics parameters remained the same as in previous simulations. The water and air mass energy-absorption coefficients averaged over the in-phantom photon energy spectrum were then calculated with `g` using the calculated in-phantom spectra in the beam source definition.

4.4 Uncertainty analysis

Type B uncertainties are non-statistical in nature and arise from uncertainty in the measurement conditions. For Monte Carlo simulations, type B uncertainties arise from potential differences between the measurement and simulation conditions. Examples of such differences are the field size and photon spectrum. There is no exact method for determining the type B uncertainties on Monte Carlo calculations. For any calculated quantity to be considered meaningful in any manner, type B uncertainties should be assigned to it. In this section, the type B uncertainties on the calculated absorbed dose to water-to-air kerma ratios, $D_{w,z=2cm}/K_a$, and the calculated ionization chamber correction factors, $P_{Q,cham}P_{sheath}$ are estimated. The method used to determine these uncertainties has been used by Wulff *et. al.* [64] and Krauss *et. al.* [22].

4.4.1 Absorbed dose to water to air kerma ratios

There are four main contributions to the type B uncertainty on the calculated $D_{w,z=2cm}/K_a$ values. They are (1) the photon spectrum, (2) the field size at the reference point, (3) the field homogeneity and (4) the photon cross sections. The methods to evaluate each contribution are discussed below.

1. To determine the type B uncertainty from the photon spectrum, additional simulations for $D_{w,z=2cm}$ and K_a were run using the *Spk*-calculated photon spectra. The standard deviation between the *Spk*-based ratios and measured spectra-based ratios is taken to be the standard uncertainty, denoted as u(spec.).

2. For the field size contribution, additional $D_{w,z=2cm}$ simulations were run with the diameter of the field at the reference point made 1 mm smaller (9.75 cm) or larger (9.95 cm) in diameter. For each modified simulation, the absolute percent difference was taken relative

to the $D_{w,z=2cm}$ value calculated with the 9.85 cm field size. The average of the percent differences was taken to be the standard uncertainty, denoted as $u(\text{FS})$. The air kerma K_a is not affected by such small changes in the field size and no additional simulations were run for it.

3. In the MC simulations, the fluence is assumed homogeneous across the surface of the phantom irradiated by the x-ray beam. This is because the photon spectrum used in the beam source definition contains no spatial information. In reality, the fluence is heterogeneous across the surface due to the Heel effect. It is estimated by Krauss *et. al* that a heterogeneous x-ray field can cause $D_{w,z=2cm}$ to change by 0.2% from its value with an assumed homogeneous field [22]. This percent change was taken to be the standard uncertainty, denoted as $u(\text{FH})$.

4. The MC simulations use only one photon cross section database (from Sabbatucci & Salvat [30], EGSnrc option `mcdf-xcom` for `photon cross sections` in the transport parameters). Of course, these cross sections are based on theory and are not completely accurate. An uncertainty on the cross sections can be determined by comparing various databases. From this uncertainty, the cross section contribution to the type B uncertainty on $D_{w,z=2cm}/K_a$ can be determined. This is done according to the following method. First, the uncertainty on the cross section of photon interaction i, $u(\sigma_i)$, is determined. Then, additional simulations for the quantity f are run with scaled photon cross sections for interaction i. The uncertainty on f due to the uncertainty on the cross section of interaction i, $u_{\sigma_i}(f)$, is then

$$u_{\sigma_i}(f) = \left| \frac{\Delta f/f}{\Delta\sigma_i/\sigma_i} \right| u(\sigma_i) \ = |s_{\sigma_i}(f)| \ u(\sigma_i), \tag{4.5}$$

where Δf is the difference in f with scaled and non-scaled cross sections and $\Delta\sigma_i$ is the difference between the scaled and non-scaled cross sections. Note that the f in the denominator of Equation 4.5 is evaluated for non-scaled photon cross sections. If the cross sections are scaled by a factor a, then $\Delta\sigma_i/\sigma_i = a - 1$. The quantity $s_{\sigma_i}(f)$ is called the sensitivity coefficient. This method is essentially error propagation but with the derivatives approximated by small, finite changes.

This method is performed for air and water photoelectric (PE) and Compton cross sections. A Python (V3.7.1) script was written to perform all of the calculations. For each interaction and medium, various data sets were analyzed to determine the uncertainty on the cross section. For the photoelectric effect, the tables "Storm and Israel (1970)", "Scofield renormalized" and "Chantler *et. al.* (2005)" from the ICRU Report 90 were considered. Additionally, the renormalized (`mcdf-xcom`) and non-renormalized (`XCOM`) data sets supplied with EGSnrc were considered. For the Compton effect, the tables "XCOM", "*Ab initio* (RIA)" and "PENELOPE" from ICRU 90 were considered along with the Compton cross sections supplied with EGSnrc. For a given interaction and medium, the respective data sets were used as samples to calculate the Student t 95% confidence interval, $u_E(\sigma_i)$, at every energy E. The final uncertainty on the cross section, $u(\sigma_i)$, was then obtained by weighting $u_E(\sigma_i)$ by the photon energy fluence spectrum at that energy, $\Psi_E(E)$, and integrating over all energies present in the spectrum, i.e.,

$$u(\sigma_i) = \frac{\int_0^{E_{max}} \Psi_E(E) u_E(\sigma_i) dE}{\int_0^{E_{max}} \Psi_E(E) dE} \ . \tag{4.6}$$

Spectral weighting has been used by Andreo *et. al.* [65]. It is done because each cross section uncertainty at a specific energy should contribute an amount proportional to the number of photons of that energy in the beam. The choice of energy fluence is made because it is a quantity related to the absorbed dose. Independent simulations were then run for $D_{w,z=2cm}$ with scaled photoelectric and Compton cross sections. The scaling factor a was 1.05 in both cases. The user code `egs_chamber` allows for the independent scaling of photon interaction cross sections by constant factors. The user code `g` does not have this function enabled so the photoelectric-scaled or Compton-scaled air kerma was calculated through Equation 3.7 with the interaction's respective mass energy-transfer coefficients scaled by 1.05. The sensitivity coefficients for $D_{w,z=2cm}/K_a$ could then be obtained. They were multiplied by the uncertainties on the photon cross sections in air (which were similar to those in water).

Note that all the uncertainty components discussed here cannot be summed in quadrature directly. This is because the uncertainty due to the photon cross sections is evaluated at the 95% confidence level. Every other component must therefore be multiplied by 1.96 to reach the 95% confidence level as well (this assumes these components are normally distributed). The standard uncertainty on $D_{w,z=2cm}/K_a$ is then

$$u\left(\frac{D_{w,z=2cm}}{K_a}\right)^2 = \frac{u(\mathrm{Compton})^2 + u(\mathrm{PE})^2 + 1.96^2 \cdot u(\mathrm{FS})^2 + 1.96^2 \cdot u(\mathrm{spec.})^2 + 1.96^2 \cdot u(\mathrm{FH})^2 + 1.96^2 \cdot u(\mathrm{type\ A})^2}{1.96^2} \tag{4.7}$$

4.4.2 Ionization chamber correction factors

There are four main contributions to the type B uncertainty on the calculated $P_{Q,cham}P_{sheath}$ values. They are (1) the field size at the reference point, (2) the photon spectrum, (3) the photon cross sections and (4) the chamber wall and central electrode dimensions. The methods used to determine the magnitude of these contributions are given below.

1. The uncertainty on $P_{Q,cham}P_{sheath}$ due to field size was estimated to be 0.1%, denoted as u(FS). This estimate is supported by Figure 4 in TG-61 [9].

2 & 3. First, let one type B uncertainty component be considered, say the photon cross sections. By changing the cross sections, all of the quantities in Equation 4.1 will be affected. Any changes in one quantity might be canceled out by changes in another quantity. Taking

the sum (in quadrature) of the uncertainties of each quantity in Equation 4.1 due to the cross sections would therefore overestimate the uncertainty on $P_{Q,cham}P_{sheath}$ due to the cross sections. This overestimate also occurs when considering the photon spectrum. The ideal method would be to independently re-calculate $P_{Q,cham}P_{sheath}$ with a modified field size, scaled cross sections and the *Spk* spectra and then evaluate the $P_{Q,cham}P_{sheath}$ type B uncertainties as per Section 4.4.1. This is not possible due to amount of simulations that would need to be run.

An alternative method, proposed by Burns *et. al.* [66], is to evaluate the type B uncertainties due to the photon cross sections and the photon spectrum through the analytic form of $P_{Q,cham}$ based on cavity theory. The analytical form is

$$P_{Q,cham} = \frac{\left[s_{wall,air}\beta_{wall}^{-1}\left(\overline{\mu_{en}}/\rho\right)_{air,wall}\Psi_{w,wall}\beta_w p_{cav}\right]_{w,z=2cm}}{\left[s_{wall,air}\beta_{wall}^{-1}\left(\overline{\mu_{en}}/\rho\right)_{air,wall}\Psi_{air,wall}(1-g_{air})^{-1}p_{cav}\right]_{air}}\ . \tag{4.8}$$

In Equation 4.8, $s_{wall,air}$ is the chamber wall material-to-air stopping power ratio, $(\mu_{en}/\rho)_{air,wall}$ is the mean wall-to-air mass-energy absorption coefficient ratio averaged over the photon energy fluence spectrum, $\Psi_{air,wall}$ is the air-to-wall energy fluence ratio and p_{cav} is a perturbation factor to account for deviations from Bragg-Gray conditions. The braces $[\ ]_{w,z=2cm}$ and $[\ ]_{air}$ indicate the quantities within should be evaluated at the reference point in a water phantom at a depth of 2 cm and free-in-air, respectively. Equation 4.8 does not take into account P_{sheath}. This is not an issue because P_{sheath}=1 for most chambers in this study. Equation 4.8 is derived from a cavity theory approach to determining the absorbed dose to water and air kerma with an air-filled cavity ionization chamber. The ratio of the resulting equations for the absorbed dose to water and air kerma is taken, much like in Equation 4.1. See Andreo *et. al.* [36] for a full derivation of these equations.

When considering the photon cross sections and the photon spectra, the quantities most affected are the mass-energy absorption coefficient ratios. As a first order approximation, the equation reduces to

$$P_{Q,cham} \approx \frac{\left[(\overline{\mu_{en}}/\rho)_{air,wall}\right]_{w,z=2cm}}{\left[(\overline{\mu_{en}}/\rho)_{air,wall}\right]_{air}} \tag{4.9}$$

To evaluate the type B uncertainty on $P_{Q,cham}$ due to the PE and Compton photon cross sections, the quantity in Equation 4.9 was evaluated for each data set listed above in Section 4.4.1. The chamber wall material was taken as graphite. For the in-air quantity, the average was taken over the measured photon spectrum. For the in-water quantity, the average was taken over the calculated photon spectrum in-phantom at a depth of 2 cm from Section 4.3.4. For each interaction, the Student t 95% confidence interval was taken and used as the cross section contribution to the uncertainty on $P_{Q,cham}$. The maximum uncertainty out of all the beam qualities is used in Table 5.3.

For the uncertainty due to the photon spectrum, the quantity in Equation 4.9 was calculated with the measured spectra and the *Spk*-calculated spectra. To obtain the in-phantom *Spk* spectra, the in-air spectra were transported through water to a depth of 2 cm at the reference point with the user code `flurznrc`. The standard deviation between the measured spectra-based value and *Spk*-based value was used as the standard uncertainty. The maximum uncertainty out of all the beam qualities is used in Table 5.3.

4. Due to the manufacturing process of the ionization chambers, the dimensions of the chamber wall and the central electrode will never be equal to the blueprint dimensions. For kilovoltage x-ray beams, the response of the chamber is especially sensitive to the diameter of the central electrode [67]. It is necessary to consider how variations in the dimensions of these chamber components can manifest as type B uncertainties on $P_{Q,cham}$. Additional in-air and in-phantom `egs_chamber` simulations were run with the PTW TM30013 model

but with the central electrode diameter increased by +0.04 mm. The uncertainty in $P_{Q,cham}$ due to the change in the electrode diameter, u(electrode), is calculated as

$$u(\text{electrode}) = \left| \frac{\Delta P_{Q,cham}/P_{Q,cham}}{\Delta d/d} \right| \frac{\sigma_d}{d} = \left| \frac{\Delta(\frac{D_{cav,a}}{D_{cav,w}})/(\frac{D_{cav,a}}{D_{cav,w}})}{\Delta d/d} \right| \frac{\sigma_d}{d} \tag{4.10}$$

where σ_d/d is the relative standard uncertainty in the diameter d and Δd is the change in diameter, +0.04 mm. In Equation 4.10, the relative change in $P_{Q,cham}$, $\Delta P_{Q,cham}/P_{Q,cham}$, is equal to the relative change in the air-to-water cavity dose ratio, $\Delta(\frac{D_{cav,a}}{D_{cav,w}})/(\frac{D_{cav,a}}{D_{cav,w}})$, through Equation 4.1. It is assumed the electrode diameter is distributed according to a symmetric triangular distribution with the blueprint diameter as the mean. Based on discussions with Standard Imaging, the electrode diameter can vary by ±0.051 mm. The bounds of the triangular distribution are then [d-0.051 mm, d+0.051 mm]. The uncertainty on the diameter, σ_d, is then 0.051 mm/$\sqrt{6}$. These simulations were run only for the 50, 100 and 140 kV beams. The largest u(electrode) (140 kV) is chosen as the standard uncertainty and is given in Table 5.3.

The uncertainty on $P_{Q,cham}$ due the change in the outer diameter of the chamber wall, u(wall), was calculated in a similar manner as in the case of the central electrode. Additional in-air and in-phantom simulations for the NE2571, PTW TM30013 and A12 chambers were run with the outer diameter of the chamber wall increased by +0.04 mm. These chambers were chosen because their walls are made of different materials. These simulations were run for 100 kV beam only. The largest u(wall) out of all the chambers (A12) was selected as the standard uncertainty and is given in Table 5.3.

References

8. IAEA. *Absorbed Dose Determination in External Beam Radiotherapy: An International Code of Practice for Dosimetry Based on Standards of Absorbed Dose to Water. Technical Report Series* **398** (IAEA, Vienna, Austria, 2001).

9. Ma, C.-M. *et al.* AAPM protocol for 40–300 kV x-ray beam dosimetry in radiotherapy and radiobiology. *Medical Physics* **28(6),** 868–893 (2001).

10. Prepared by a Working Party of the (Chair) and Aukett, R. J., Harrison, R. M., Moretti, C., Nahum, A. E. & Rosser, K. E. The IPEMB code of practice for the determination of absorbed dose for x-rays below 300 kV generating potential (0.035 mm Al - 4 mm Cu HVL; 10 - 300 kV generating potential). *Physics in Medicine and Biology* **41(12),** 2605–2625 (1996).

11. Grimbergen, T. W. M. *et al. NCS Report 10: Dosimetry of low and medium energy X-rays* **10** (NCS, Delft, The Netherlands, 1997).

18. Seltzer, S. M. *et al.* ICRU Report 90. Key data for ionizing-radiation dosimetry: Measurement standards and applications. *Journal of the International Commission on Radiation Units and Measurements* **14(1)** (2016).

22. Krauss, A., Büermann, L., Kramer, H. M. & Selbach, H. J. Calorimetric determination of the absorbed dose to water for medium-energy x-rays with generating voltages from 70 to 280 kV. *Physics in Medicine and Biology* **57(19),** 6245–6268 (2012).

30. Sabbatucci, L. & Salvat, F. Theory and calculation of the atomic photoeffect. *Radiation Physics and Chemistry* **121,** 122–140 (2016).

36. Andreo, P., Burns, D. T., Nahum, A. E., Seuntjens, J. & Attix, F. H. *Fundamentals of Ionizing Radiation Dosimetry* 2nd ed. (Wiley, 2017).

54. Andreo, P. Monte Carlo techniques in medical radiation physics. *Physics in Medicine and Biology* **36(7),** 861–920 (1991).

55. Kawrakow, I., Mainegra-Hing, E., Rogers, D. W. O., Tessier, F. & Walters, B. R. B. *The EGSnrc code system: Monte Carlo simulation of electron and photon transport* tech. rep. PIRS-701 (National Research Council Canada, 2017). `http://nrc-cnrc.github.io/EGSnrc/doc/pirs701-egsnrc.pdf`.
56. Kawrakow, I., Mainegra-Hing, E., Tessier, F., Townson, R. & Walters, B. R. B. *EGSnrc C++ class library* tech. rep. PIRS-898 (National Research Council Canada, 2018). `https://nrc-cnrc.github.io/EGSnrc/doc/pirs898/index.html`.
57. Wulff, J., Zink, K. & Kawrakow, I. Efficiency improvements for ion chamber calculations in high energy photon beams. *Medical Physics* **35(4),** 1328–1336 (2008).
58. Kawrakow, I. Accurate condensed history Monte Carlo simulation of electron transport. I. EGSnrc, the new EGS4 version. *Medical Physics* **27(3),** 485–498 (2000).
59. Ketelhut, S. private communication.
60. Berger, M. J., Coursey, J. S., Zucker, M. A. & Chang, J. *ESTAR, PSTAR, and ASTAR: Computer Programs for Calculating Stopping-Power and Range Tables for Electrons, Protons, and Helium Ions (version 1.2.3)* `http://physics.nist.gov/Star`. Accessed: 15/07/2019. National Institute of Standards and Technology, Gaithersburg, MD, 2005.
61. Sechopoulos, I. *et al.* RECORDS: improved Reporting of montE CarlO RaDiation transport Studies: Report of the AAPM Research Committee Task Group 268. *Medical Physics* **45(1),** e1–e5 (2018).
62. Andreo, P. private communication.
63. Poludniowski, G., Landry, G., DeBlois, F., Evans, P. M. & Verhaegen, F. SpekCalc: a program to calculate photon spectra from tungsten anode x-ray tubes. *Physics in Medicine and Biology* **54(19),** N433–N438 (2009).

64. Wulff, J., Heverhagen, J. T., Zink, K. & Kawrakow, I. Investigation of systematic uncertainties in Monte Carlo-calculated beam quality correction factors. *Physics in Medicine and Biology* **55(16),** 4481–4493 (2010).

65. Andreo, P., Burns, D. T. & Salvat, F. On the uncertainties of photon mass energy-absorption coefficients and their ratios for radiation dosimetry. *Physics in Medicine and Biology* **57(8),** 2117–2136 (2012).

66. Burns, D. T., Kessler, C. & Roger, P. *New BIPM absorbed dose standard for medium energy x-rays* (CCRI, BIPM, Sèvres, France, 2017). `https://www.bipm.org/cc/AllowedDocuments.jsp?cc=CCRI(I)`.

67. Ubrich, F., Wulff, J., Kranzer, R. & Zink, K. Thimble ionization chambers in medium-energy x-ray beams and the role of constructive details of the central electrode: Monte Carlo simulations and measurements. *Physics in Medicine and Biology* **53(18),** 4893–4906 (2008).

Chapter 5

Results and Discussion

5.1 Absorbed dose to water and air kerma

The results of the absorbed dose to water simulations (Section 4.3.2) and the air kerma simulations (Section 4.3.4) are combined to give the ratio of the absorbed dose to water at a depth of 2 cm and the air kerma, $D_{w,z=2cm}/K_a$. This ratio is one component in calculating the chamber correction factors with Equation 4.1. The simulation results (MC) for $D_{w,z=2cm}/K_a$ are given in Figure 5.1. The ratios are given as a function of the radiation beam quality in mm Cu (Table 4.2). The combined type A and type B uncertainties (k=1) on the calculated ratios decrease from 0.6% to 0.3% with increasing beam quality. The methods for estimating the type B uncertainties are discussed in Section 4.4. Experimental results for $D_{w,z=2cm}/K_a$ measured by PTB are also shown in Figure 5.1. The absorbed dose to water at a depth of 2 cm was determined with their kilovoltage beam water calorimetry-based absorbed dose to water primary standard. The air kerma was determined with their free air chamber-based air kerma primary standard. The uncertainties (k=1) on the PTB results are taken from Table 4 in the article by Krauss with an additional uncertainty of 0.26% to account for the uncertainty in the air kerma measurements [22]. The experimental uncertainties vary from 1% to 0.5% with increasing beam quality. At the k=1 level of uncertainty, there is a clear discrepancy between the simulated and measured values of $D_{w,z=2cm}/K_a$ at 50 kV and 100-200 kV. There seems to be much better agreement for the higher energy beams (250, 280 and 300 kV) and 70 kV. There is agreement between the simulated and experimental values at the k=2 level for all beam qualities, except at 150 kV.

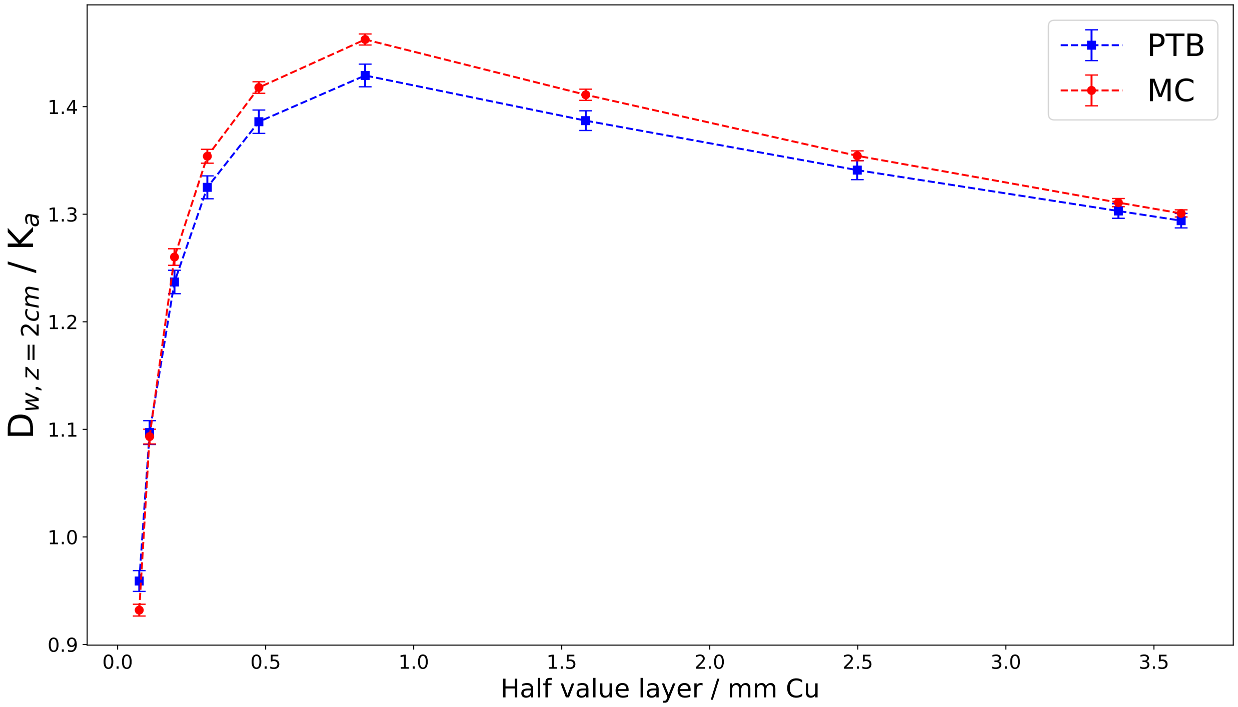

Figure 5.1 – Simulation (MC) and experimental (PTB) results for $D_{w,z=2cm}/K_a$, the ratio of the absorbed dose to water at a depth of 2 cm and air kerma. The ratio is given as a function of radiation beam quality in mm Cu. The total uncertainty on the simulated values varies from 0.6% to 0.3% (k=1). The uncertainty on the experimental values varies from 1% to 0.5% (k=1).

5.2 Water-to-air mass-energy absorption coefficient ratios

Figure 5.2 summarizes the simulation results (MC) of $\left[(\overline{\mu_{en}}/\rho)_{w,a}\right]_{w,Q,z=2cm}$, the water-to-air mass-energy absorption coefficient ratio averaged over the photon energy fluence spectrum at a depth of 2 cm in a water phantom. This quantity was determined according to Section 4.3.4. The uncertainty on these values due to the photon spectrum is 0.11% (k=1). Calculations carried out by PTB in a similar manner with EGSnrc and non-renormalized cross sections yielded similar results [68]. It is interesting to see that the difference is small between the water-to-air mass-energy absorption coefficient ratios calculated with non-normalized cross sections and those calculated with renormalized cross sections (MC vs PTB). This is an expected result. As shown in the ICRU Report 90 and a study by Andreo *et. al.* [65], even though the water and air renormalized cross sections differ by about -2% from the non-normalized cross sections, taking the ratio of the water and air attenuation coefficients eliminates this difference (above photon energies of about 4 keV). The values given in the AAPM TG-61 protocol are also shown and have an associated uncertainty of 1.5% (k=1) [9]. The TG-61 values were calculated using the EGS4 Monte Carlo code and non-renormalized cross sections [69]. Apart from the differences in the photon spectra (beam qualities), the differences between the MC/PTB values and the TG-61 values can be attributed to the handling of Compton scattering in the EGSnrc code (RIA) vs the EGS4 code (Klein-Nishina).

5.3 Ionization chamber correction factors

This section presents the simulation results for the chamber correction factors for the ionization chambers listed in Table 4.3. They are calculated using Equation 4.1 with each component simulated according to Chapter 4. In Section 5.3.1, the simulation results are

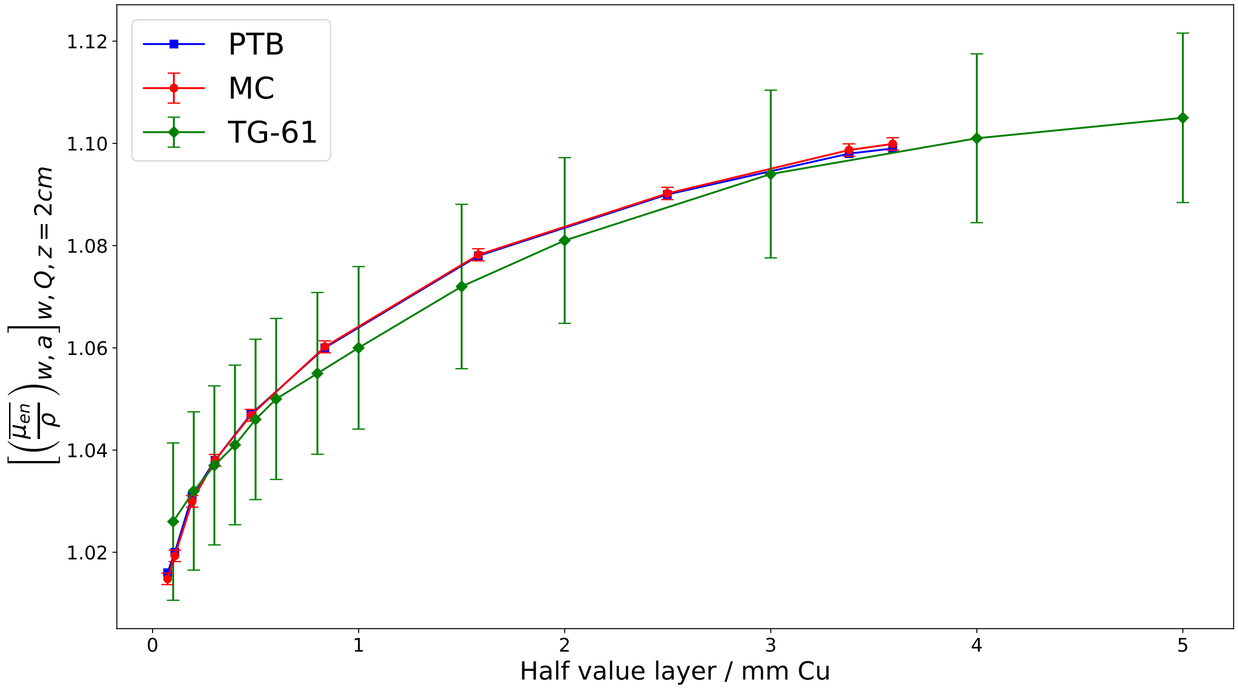

Figure 5.2 – Simulation (MC) results for $\left[(\overline{\mu_{en}}/\rho)_{w,a}\right]_{w,Q,z=2cm}$, the water-to-air mass-energy absorption coefficient ratio averaged over the photon energy fluence spectrum at a depth of 2 cm in a water phantom. The uncertainty due to the photon spectra is 0.11% (k=1). Similar calculations done by PTB are shown in blue. The values reported by the AAPM TG-61 protocol are shown in green and have an associated uncertainty of 1.5% (k=1).

compared with the experimental chamber correction factors obtained by PTB with their absorbed dose to water calorimeter primary standard. In Section 5.3.2, the calculated chamber correction factors are compared to those determined by national metrology institutes and the International Bureau of Weights and Measures (BIPM).

5.3.1 Comparisons with PTB

The calculated kilovoltage beam chamber correction factors for the chambers listed in Table 4.3 are shown in Figures 5.3 to 5.7 (MC). They are given as a function of the beam quality in mm Cu. The uncertainty on the calculated values at k=1 is 0.3%. Note that the overall chamber correction factor, $P_{Q,cham}$, is the quantity calculated except for the NE2571 where $P_{Q,cham}P_{sheath}$ is calculated. For all beam qualities, the correction factor is within 3.1% of unity. The methods for uncertainty analysis are discussed in Section 4.4. The measured correction factors obtained at PTB are also shown with an uncertainty of 1% at k=1 [22, 68]. The measured correction factors are much closer to unity and do not vary as much with beam quality. There are clear discrepancies between the calculated and measured correction factors. Investigations into these discrepancies are addressed in Section 5.5. The chamber correction factors for the NE2571 and Exradin A12 chambers given in TG-61 are shown in Figure 5.4 and 5.7, respectively. The standard uncertainty on the TG-61 factors is 1.5%.

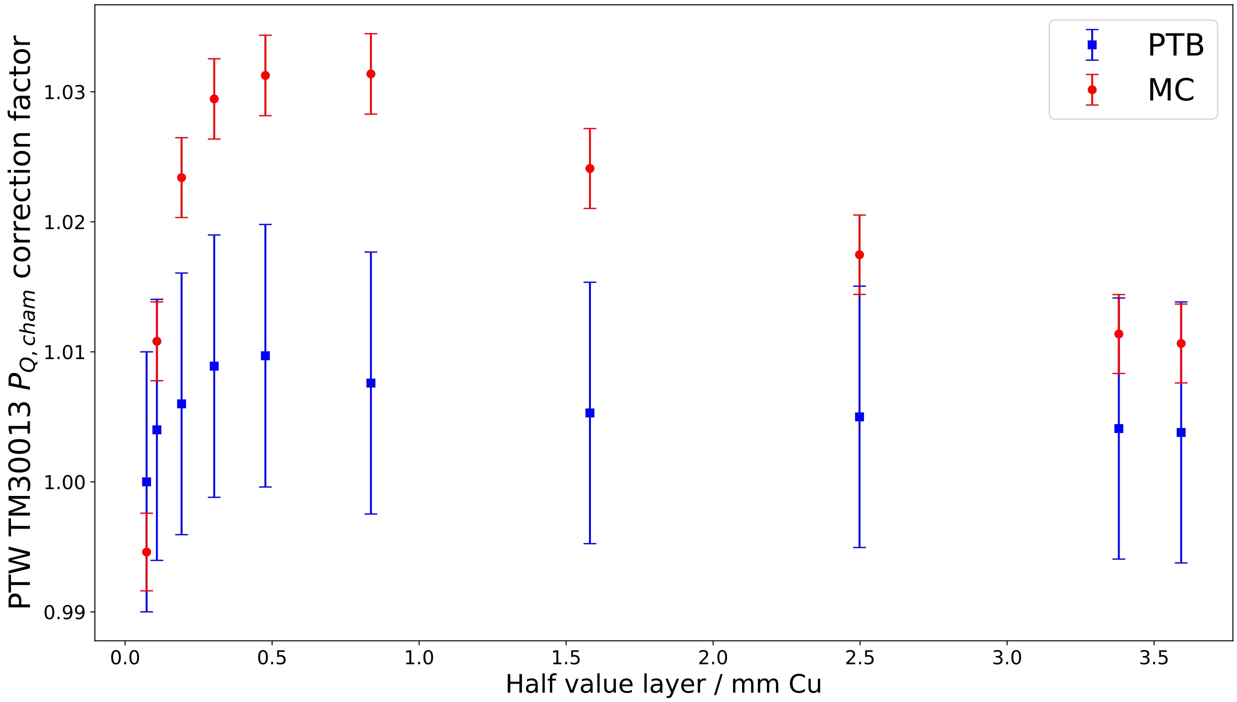

Figure 5.3 – Calculated (MC) and measured (PTB) overall chamber correction factors for the PTW TM30013 chamber. The standard uncertainty is 0.3% on the calculated factors and 1% on the measured factors.

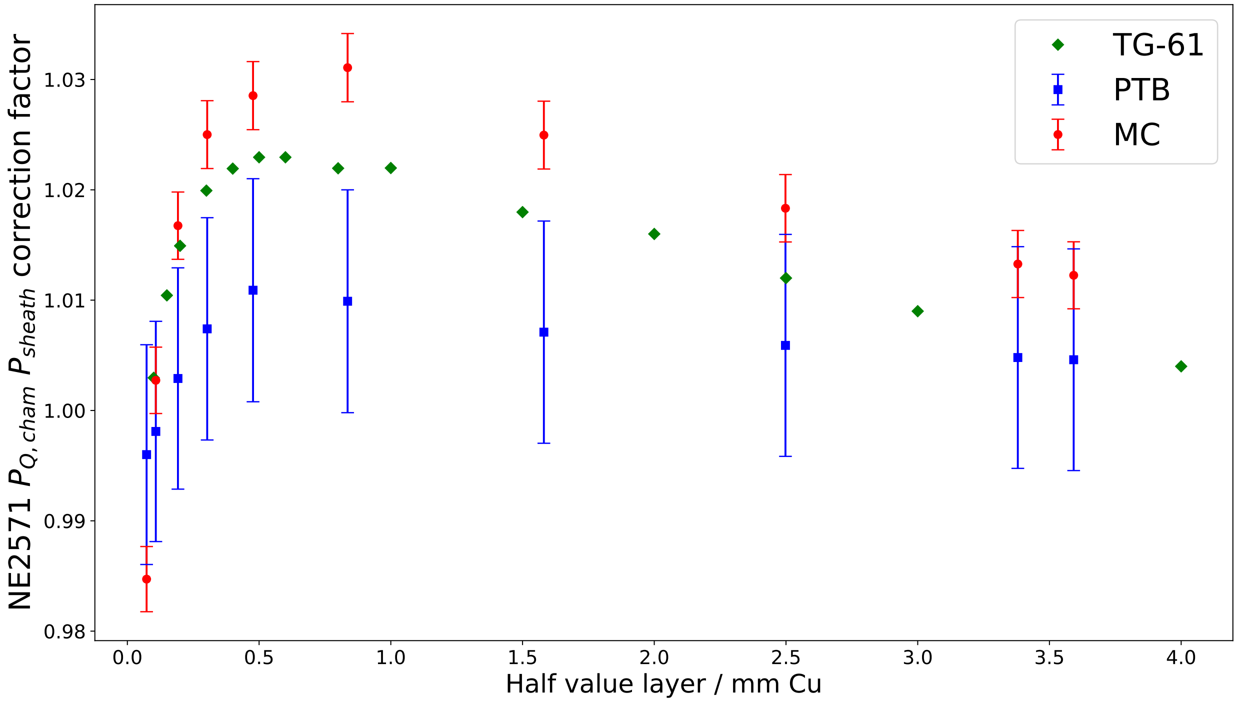

Figure 5.4 – Calculated (MC), measured (PTB) and TG-61 chamber correction factors for the NE2571 chamber. The standard uncertainty is 0.3% on the calculated factors and 1% on the measured factors.

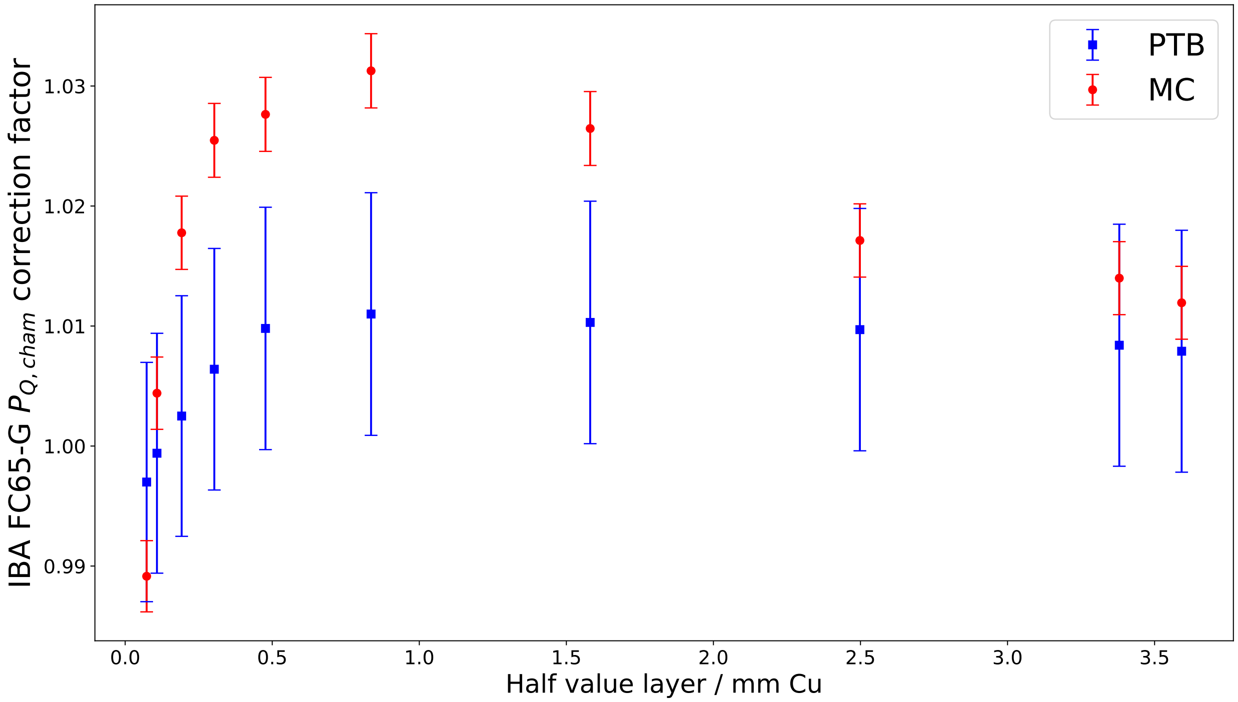

Figure 5.5 – Calculated (MC) and measured (PTB) overall chamber correction factors for the IBA FC65-G chamber. The standard uncertainty is 0.3% on the calculated factors and 1% on the measured factors.

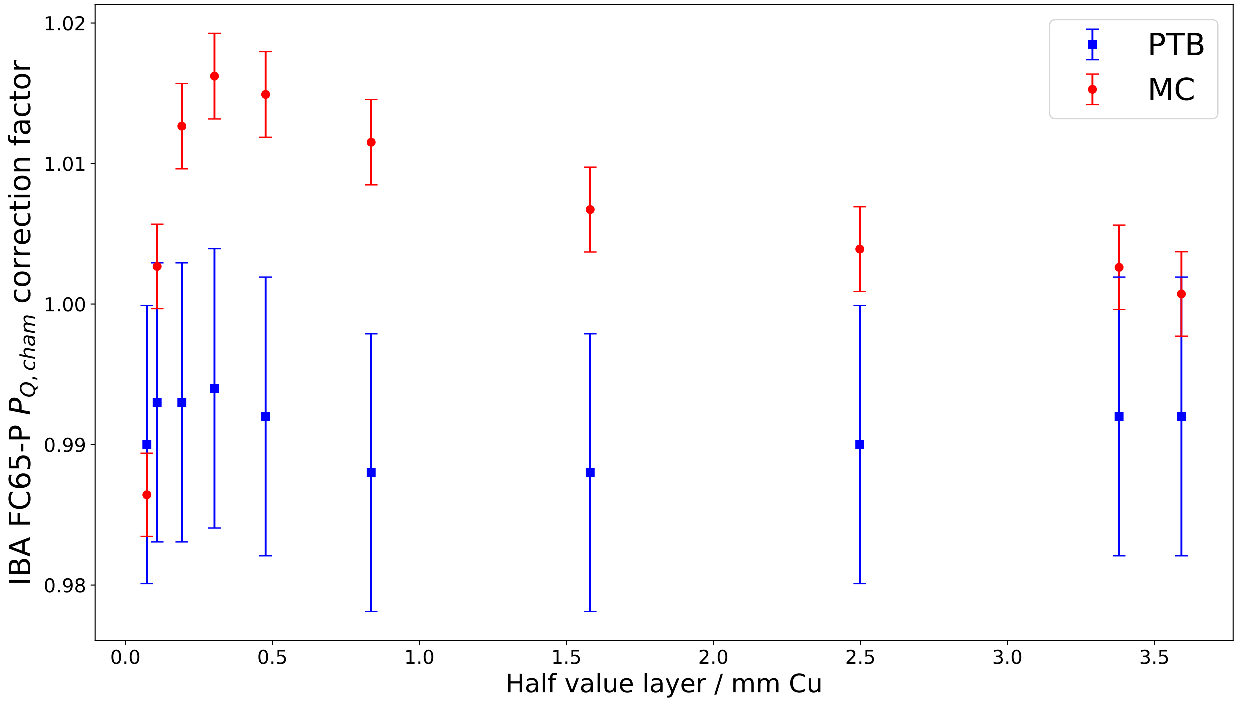

Figure 5.6 – Calculated (MC) and measured (PTB) overall chamber correction factors for the IBA FC65-P chamber. The standard uncertainty is 0.3% on the calculated factors and 1% on the measured factors.

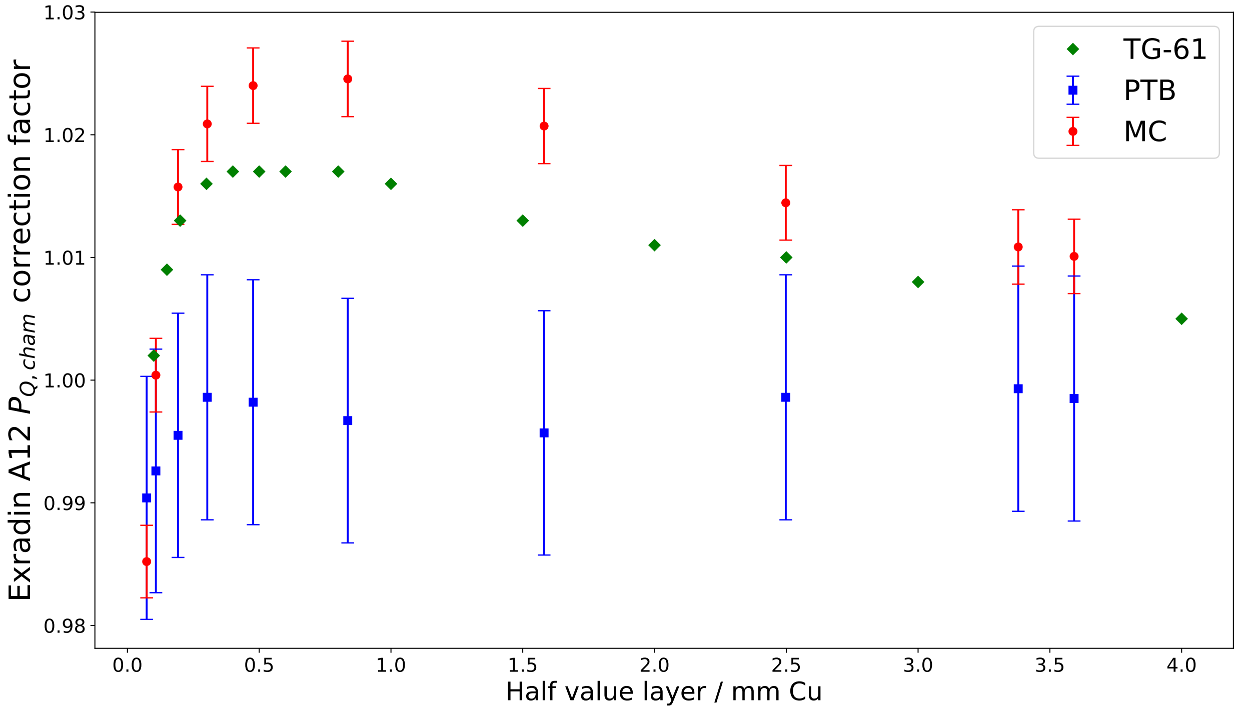

Figure 5.7 – Calculated (MC), measured (PTB) and TG-61 overall chamber correction factors for the Exradin A12 chamber. The standard uncertainty is 0.3% on the calculated factors and 1% on the measured factors.

5.3.2 International comparisons

Due to the recent development of kilovoltage beam absorbed dose to water primary standards, key comparisons between national metrological institutes have been conducted. One such key comparison, designated as EURAMET.RI(I)-S13, was organized by the European Association of National Metrology Institutes (EURAMET) and was completed in 2016 [68]. Four national metrological institutes participated in this comparison; PTB (Germany), VSL (Netherlands), ENEA-INMRI (Italy) and LNE-LNHB (France). Of the four participants, three participants (PTB, VSL and LNE-LNHB) used water calorimetry-based absorbed dose to water primary standards while the ENEA used a graphite calorimetry-based primary standard. In this comparison, the overall chamber correction factor for the PTW TM30013 was determined by all institutions. The results of this comparison are shown in Figure 5.8. It should be noted that this comparison used the CCRI beam qualities which are different than those used in the MC simulations. The tube potentials for the CCRI qualities are indicated next to the data points from the comparison.

The BIPM has also developed their own kilovoltage beam absorbed dose to water primary standard. It is based on an existing air kerma primary standard and Monte Carlo calculations [66]. With this primary standard, the absorbed dose to water at a depth of 2 cm in a water phantom, $D_{w,z=2cm}$, is derived using the following equation

$$D_{w,z=2cm} = K_a \frac{M_w}{M_a} k_r \left(\frac{D_{w,z=2cm}/D_{cav,w}}{K_a/D_{cav,a}} \right)_{MC} . \tag{5.1}$$

In Equation 5.1, the quantity in parentheses is Monte Carlo calculated using the PENELOPE code system [70]. It is essentially the ratio of the absorbed dose to water and air kerma calibration coefficients. The MC calculated dose to water at a depth of 2 cm, $D_{w,z=2cm,MC}$, is calculated over the dimensions of the chamber cavity. The measured correction factor k_r corrects for radial dose non-uniformity over the dimensions of the chamber cavity. The quantities M_w and M_a are measured chamber readings in-phantom and in-air, respectively. The quantities $D_{cav,w}$ and $D_{cav,a}$ are the MC calculated chamber cavity doses in-phantom and in-air, respectively. Air kerma, K_a, is measured with their free air chamber primary standard. Comparing Equation 5.1 to Equation 1.5, it can be seen that

$$k_r \left(\frac{D_{w,z=2cm}/D_{cav,w}}{K_a/D_{cav,a}} \right)_{MC} = \left[\left(\frac{\overline{\mu_{en}}}{\rho} \right)_{w,a} \right]_{w,Q,z=2cm} P_{Q,cham} P_{sheath} . \tag{5.2}$$

As can be seen in Equation 5.2, the BIPM calculated chamber correction factor can be extracted upon dividing the left hand side by the water-to-air mass-energy absorption coefficient ratio. In the initial study of this primary standard by the BIPM [66], the Exradin A12 and PTW TM30013 were used. The CCRI radiation qualities were used as well. The CCRI quality water-to-air mass-energy absorption coefficient ratios were looked up in the kV data prepared by Andreo [71] to obtain the chamber correction factors through Equation 5.2. The results for the PTW TM30013 and the Exradin A12 are shown in Figures 5.8 and 5.9, respectively. The standard uncertainty on the BIPM values is 0.42%.

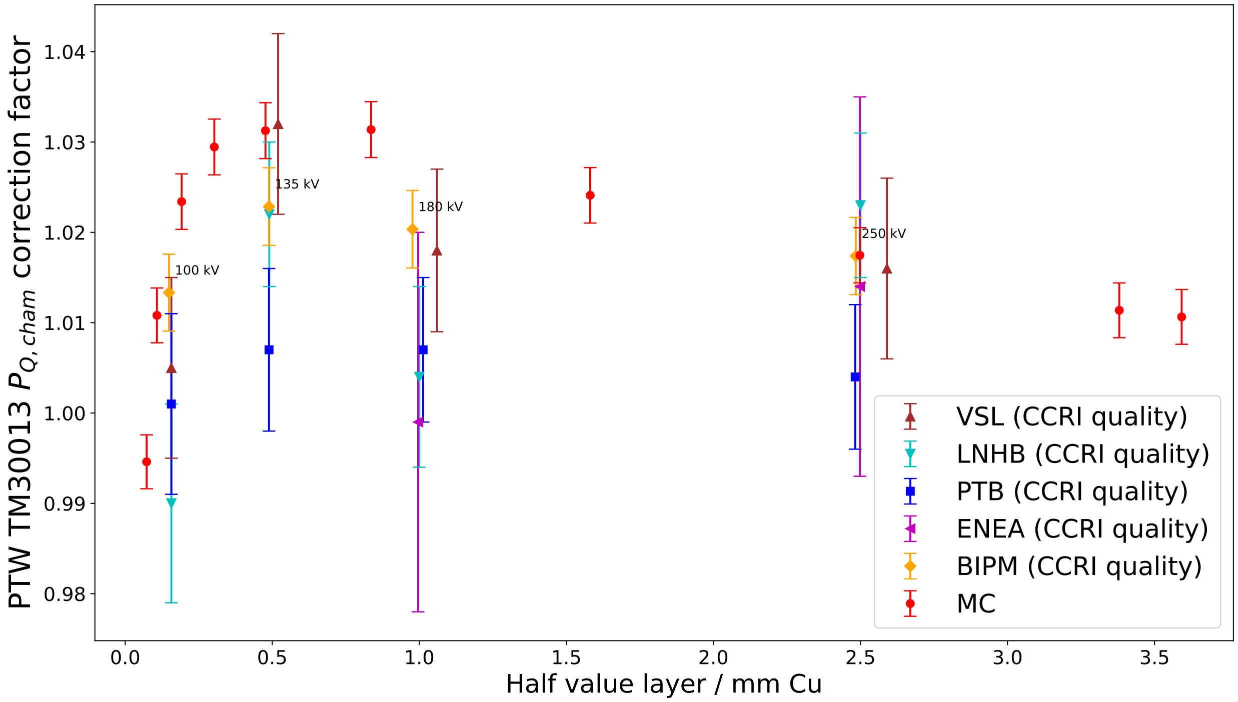

Figure 5.8 – The overall chamber correction factor for the PTW TM30013 chamber. The BIPM factors determined with their primary standard are given in yellow with a standard uncertainty of 0.42%. The chamber correction factors measured by several national metrological institutes (EURAMET.RI(I)-S13) with their primary standards are shown. The standard uncertainties on the EURAMET values are on the order of 1%, expect for the ENEA-INMRI where the standard uncertainty is 2.1%. The MC calculated correction factors have already been presented. The BIPM and EURAMET factors are determined for the CCRI beam qualities. The CCRI quality tube potentials are labelled next to the data points.

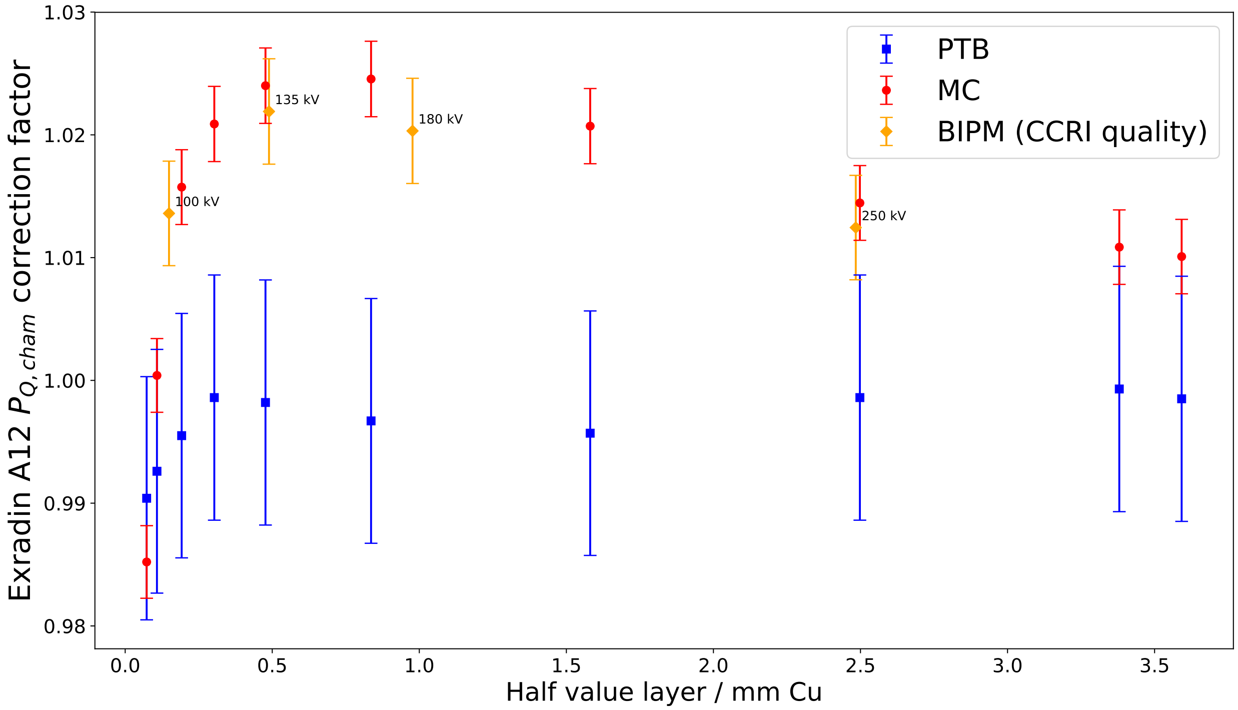

Figure 5.9 – The overall chamber correction factor for the Exradin A12 chamber. The BIPM factors determined with their primary standard are given in yellow with a standard uncertainty of 0.42%. The MC calculated correction factors have already been presented. The BIPM factors are determined for the CCRI beam qualities. The CCRI quality tube potentials are labelled next to the data points.

5.4 Uncertainty analysis

5.4.1 Absorbed dose to water to air kerma ratios

The uncertainty contributions to $D_{w,z=2cm}/K_a$ for each beam quality are listed in Table 5.2 along with the standard uncertainty $u(D_{w,z=2cm}/K_a)$. These were determined according to the methods of Section 4.4.1. The type A statistical uncertainties from the MC simulations are also given.

In comparison to the type B uncertainties in Table 6 of Krauss *et. al.* [22], the uncertainties calculated here are smaller by a factor of two. This is because the uncertainties on the

kV	50	70	100	120	140	150	200	250	280	300
$u(\sigma_{\text{PE}})$ (air) (95% CI)	1.42	1.32	1.25	1.26	1.42	1.55	1.71	1.71	1.73	1.75
$u(\sigma_{\text{Compton}})$ (air) (95% CI)	1.11	0.95	0.81	0.75	0.70	0.64	0.57	0.53	0.50	0.50
$s_{\text{PE}}(D_{w,z=2cm}/K_a)$	-0.24	-0.34	-0.24	-0.18	-0.094	-0.024	0.013	0.030	0.004	0.007
$s_{\text{Compton}}(D_{w,z=2cm}/K_a)$	0.13	0.20	0.22	0.18	0.18	0.15	0.12	0.11	0.077	0.081

Table 5.1 – Uncertainties on the photoelectric and Compton cross sections. They are multiplied by the respective sensitivity coefficients to obtain the uncertainty on $D_{w,z=2cm}/K_a$ due to the photon cross sections.

kV	50	70	100	120	140	150	200	250	280	300
type A	0.1	0.1	0.1	0.1	0.1	0.1	0.1	0.1	0.1	0.1
$u_{\text{PE}}(D_{w,z=2cm}/K_a)$ (95% CI)	0.34	0.45	0.30	0.22	0.13	0.038	0.023	0.052	0.007	0.012
$u_{\text{Compton}}(D_{w,z=2cm}/K_a)$ (95% CI)	0.14	0.19	0.18	0.13	0.12	0.096	0.069	0.056	0.039	0.041
u(spec.)	0.50	0.50	0.50	0.34	0.12	0.16	0.14	0.082	0.001	0.001
u(FS)	0.13	0.19	0.24	0.23	0.28	0.24	0.27	0.26	0.21	0.16
u(FH)	0.2	0.2	0.2	0.2	0.2	0.2	0.2	0.2	0.2	0.2
$u(D_{w,z=2cm}/K_a)$ (k=1)	0.60	0.64	0.62	0.49	0.39	0.36	0.38	0.35	0.31	0.27

Table 5.2 – Uncertainty components contributing to the total uncertainty on $D_{w,z=2cm}/K_a$, $u(D_{w,z=2cm}/K_a)$. The components are combined according to Equation 4.7.

photon cross sections estimated here are smaller.

5.4.2 Ionization chamber correction factors

The uncertainty contributions to $P_{Q,cham}P_{sheath}$ for each beam quality are listed in Table 5.3 along with the standard uncertainty $u(P_{Q,cham}P_{sheath})$. These were determined according to the methods of Section 4.4.2.

5.5 Discussion

As seen in Figure 5.1, there is a discrepancy between the measured and calculated absorbed dose to water-to-air kerma ratios, $D_{w,z=2cm}/K_a$. Table 5.4 gives the percent differences

kV	50	70	100	120	140	150	200	250	280	300
type A	0.1	0.1	0.1	0.1	0.1	0.1	0.1	0.1	0.1	0.1
$u_{\text{PE}}(P_{Q,cham})$ (95% CI)	0.005	0.009	0.008	0.009	0.011	0.013	0.010	0.007	0.005	0.005
$u_{\text{Compton}}(P_{Q,cham})$ (95% CI)	0.008	0.004	0.021	0.055	0.096	0.14	0.067	0.010	0.062	0.069
u(spec.)	0.062	0.062	0.062	0.034	0.015	0.008	0.001	0.005	0.005	0.005
u(FS)	0.1	0.1	0.1	0.1	0.1	0.1	0.1	0.1	0.1	0.1
u(wall)	0.10	0.10	0.10	0.10	0.10	0.10	0.10	0.10	0.10	0.10
u(electrode)	0.2	0.2	0.2	0.2	0.2	0.2	0.2	0.2	0.2	0.2
$u(P_{Q,cham})$ (k=1)	0.27	0.27	0.28	0.27	0.27	0.27	0.27	0.26	0.27	0.27

Table 5.3 – Components that contribute to the total standard uncertainty on $P_{Q,cham}$, $u(P_{Q,cham})$. The uncertainty components are summed in a similar fashion to Equation 4.7.

between the calculated and measured ratios for each beam quality. The discrepancy is especially apparent at 50 kV and between 100-200 kV. Modified simulations were used to investigate the cause of this discrepancy. For the low-energy beams (50-100 kV), it was shown that the discrepancy could not be due to the measured photon spectra not being representative of the true spectra. The half-value layers for these beams were measured by PTB and found to be in agreement with the HVLs calculated from the measured spectra. The percent differences of the measured vs calculated HVLs (from 50-100 kV) are 1.4%, 0.16% and 1.9%. This indicates the measured (low energy) spectra are accurate. The use of *Spk* calculated photon spectra reduced the magnitude of the calculated ratios but not enough so as to bring them within uncertainty of the measured values. At 120 kV and above, the calculated ratios were reduced by less than 0.3%. From 50 to 100 kV, the calculated ratios were reduced by 0.9 to 0.6%. The use of non-renormalized cross sections in the simulations (XCOM database) reduced the magnitude of the calculated ratios for beam qualities up to 120 kV. With non-renormalized cross sections, the calculated ratios from 50 to 120 kV changed by -1.1%, -0.98%, -0.46% and -0.33% relative to the values calculated with renormalized cross sections. Again, these changes are not enough to bring the calculated ratios within uncertainty of the measured ratios. The PTB water calorimeter, as seen in Figure 3.4, consists not just of a water tank but of a surrounding 1 cm thick

kV	Percent difference (%)
50	2.9
70	0.34
100	-1.9
120	-2.1
140	-2.2
150	-2.3
200	-1.7
250	-0.98
280	-0.60
300	-0.52

Table 5.4 – The percent difference between the measured and calculated absorbed dose to water-to-air kerma ratio, $D_{w,z=2cm}/K_a$. The percent difference is calculated as $100 \cdot \left(\frac{measured-calculated}{calculated}\right)$. A negative percent difference indicates the calculated value is larger than the respective measured value.

PMMA enclosure. There is a 0.5 cm PMMA radiation entrance window in the path of the x-ray beam as well. In additional simulations of the dose to water at a depth of 2 cm, these calorimeter components were modelled as well as the water phantom. As such, the beam passes through 0.5 cm of PMMA and then 1.5 cm of liquid water. From 50 to 120 kV, the associated calculated ratios increase because the PMMA window attenuates photons less than the water it replaces. Therefore, more low energy photons reach the reference point and deposit dose. Apart from 50 kV, the increase in the ratio is not desirable. From 150 to 300 kV, the ratios calculated with the additional PMMA decrease with beam quality relative to the ratios calculated without the PMMA. The percent decrease varies from 0.2% to 0.35% in this beam quality range. This is not sufficient for the 150 and 200 kV beams to be brought into agreement with the measured ratios.

Any of the simulation modifications discussed in the paragraph above are not sufficient enough to obtain an agreement between the calculated and measured values of $D_{w,z=2cm}/K_a$ at the k=1 level for the 50 kV and 100-200 kV beams. Note that there is agreement between the simulated and experimental values at the k=2 level for all beam qualities, expect at 150 kV. It is also possible that there may be some systematic issues with the accuracy of the PTB water calorimeter standard. An indication of this can be seen in Figure 1 of the BIPM-PTB kilovoltage beam absorbed dose to water key comparison EURAMET.RI(I)-K9 (which includes the results of the EURAMET.RI(I)-S13 comparison) [72]. The absorbed dose to water values themselves (relative to the BIPM) differ between all institutes. It is only at the k=2 level that they agree with each other. The experimental uncertainty (k=1) in the PTB water calorimeter measurements might also need to be reevaluated and increased.

As can be seen in Figures 5.3 through 5.7, there are discrepancies at k=1 between the calculated and measured values of the chamber correction factor. These discrepancies are primarily due to similar discrepancies between the measured and simulated values of $D_{w,z=2cm}/K_a$. By combining the measured values of $D_{w,z=2cm}/K_a$ with the simulated chamber cavity doses, these "hybrid" chamber correction factors agree with the measured factors for all chambers and beam qualities within the standard uncertainty. This implies that the chamber simulations are quite accurate with respect to the chamber measurements and the discrepancy is not due to a lack of accuracy in chamber modeling. It is then worth considering if modifying the chamber simulations (PMMA enclosure, different spectra, non-renormalized cross sections), along with the $D_{w,z=2cm}/K_a$ simulations, would reduce or eliminate the discrepancy between the measured and calculated chamber correction factors. In fact, it does not. This is because any effect on $D_{w,z=2cm}/K_a$ caused by the modified simulations is canceled out by similar effects on $D_{cav,w}/D_{cav,a}$.

The PTW TM30013 chamber correction factors measured by some of the participants of the EURAMET project agree with the MC calculated factors (Figure 5.8) and only for certain beam qualities. This agreement is not strong though because the uncertainties on the measured values are quite large. The BIPM-determined chamber correction factors, shown in Figures 5.8 and 5.9, are of similar magnitude as the correction factors calculated in this thesis (MC). This demonstrates the consistency between their simulations and those done in this thesis. Any discrepancy not accounted for by uncertainty is likely due to the differences in beam quality and the chamber models.

One limitation of the ionization chamber simulations performed in this thesis is that they do not account for any chamber-to-chamber variations (except chamber wall and electrode machining tolerances which are accounted for in the uncertainty analysis). These variations include trace impurities in the material composition of the chamber wall and the construction of the chamber itself. The effect of the trace impurities on the chamber response become significant at low energies due to photoelectric absorption [73]. Therefore, for any given chamber, it will not exactly have the respective correction factors calculated in this thesis. The calculated chamber correction factors can be thought of as a limiting case, not specific to any one iteration of a chamber.

References

9. Ma, C.-M. *et al.* AAPM protocol for 40–300 kV x-ray beam dosimetry in radiotherapy and radiobiology. *Medical Physics* **28(6),** 868–893 (2001).

22. Krauss, A., Büermann, L., Kramer, H. M. & Selbach, H. J. Calorimetric determination of the absorbed dose to water for medium-energy x-rays with generating voltages from 70 to 280 kV. *Physics in Medicine and Biology* **57(19),** 6245–6268 (2012).

65. Andreo, P., Burns, D. T. & Salvat, F. On the uncertainties of photon mass energy-absorption coefficients and their ratios for radiation dosimetry. *Physics in Medicine and Biology* **57(8),** 2117–2136 (2012).

66. Burns, D. T., Kessler, C. & Roger, P. *New BIPM absorbed dose standard for medium energy x-rays* (CCRI, BIPM, Sèvres, France, 2017). `https://www.bipm.org/cc/AllowedDocuments.jsp?cc=CCRI(I)`.

68. Büermann, L. *et al.* First international comparison of primary absorbed dose to water standards in the medium-energy X-ray range. *Metrologia* **53(1A),** 06007 (2016).

69. Ma, C. M. & Seuntjens, J. P. Mass-energy absorption coefficient and backscatter factor ratios for kilovoltage x-ray beams. *Physics in Medicine and Biology* **44(1),** 131–143 (1999).

70. Salvat, F., Fernández-Varea, J. M. & Sempau, J. *PENELOPE2014, A Code System for Monte-Carlo Simulation of Electron and Photon Transport* (University of Barcelona, Barcelona, Spain, 2015). `https://www.oecd-nea.org/tools/abstract/detail/nea-1525#top`.

71. Andreo, P. Data for the dosimetry of low- and medium-energy kV x rays. *Unpublished.* `http://rgdoi.net/10.13140/RG.2.2.16558.56640` (2018).

72. Burns, D. T., Kessler, C., Büermann, L. & Ketelhut, S. Key comparison BIPM.RI(I)-K9 of the absorbed dose to water standards of the PTB, Germany and the BIPM in medium-energy x-rays. *Metrologia* **55(1A),** 06006 (2018).

73. Seuntjens, J. P., Kawrakow, I., Borg, J., Hobeila, F. & Rogers, D. W. O. *Calculated And Measured Air-Kerma Response Of Ionization Chambers In Low- And Medium-Energy Photon Beams* in *Recent Developments in Accurate Radiation Dosimetry, Proceedings of the International Workshop* (Medical Physics, Madison, WI, 2002), 69–84.

Chapter 6

Conclusion

6.1 Summary

The aim of this thesis was to calculate kilovoltage beam ionization chamber correction factors using the Monte Carlo method. These factors have not been re-examined with up-to-date Monte Carlo codes and photon and electron interaction data since the introduction of the AAPM TG-61 and IAEA TRS-398 protocols. The recent development of kilovoltage beam absorbed dose to water primary standards also now allows for the direct measurement of these correction factors. In particular, PTB has obtained experimental values for several chamber correction factors with their water calorimetry-based absorbed dose to water primary standard. Comparisons between the experimental factors obtained by PTB and calculated chamber correction factors are used as validation of the calculated factors. The planned update to the TRS-398 protocol will also include these newly-determined factors.

The kilovoltage beam ionization chamber correction factors were calculated according to Equation 4.1. Each quantity was determined through Monte Carlo simulations with the EGSnrc radiation transport toolkit. The correction factors were determined for ten kilovoltage beams of varying radiation quality (Table 4.2). These beams were also used by PTB in their experiments. The photon fluence spectra of these beams were measured by PTB and used in the beam source definition of the simulations. The absorbed dose to water at a depth of 2 cm in a water phantom at the reference point 100 cm away from the beam source was calculated with the `egs_chamber` user code. The field size was set to 9.85 cm in diameter at the reference point. Models were developed for the PTW TM30013, NE2571, IBA FC65-G, IBA FC65-P and Exradin A12 ionization chambers according to manufacturer blueprints in `egs_chamber` and were used for in-air and in-phantom simulations. The air kerma was calculated using the user code `g`. The mean water-to-air mass-energy absorption coefficient ratios averaged over the photon energy fluence spectrum at a depth of 2 cm at the reference point in the water phantom were calculated with `g` with the in-phantom photon spectra calculated with `flurznrc`.

The calculated absorbed dose to water-to-air kerma ratios deviated significantly from the PTB-measured values at 50 kV and 100-200 kV. The PTB measured this ratio with their water calorimeter and free air chamber primary standards. A detailed uncertainty analysis estimated the standard uncertainties on the calculated ratios to range from 0.6 to 0.3% with increasing beam quality. The field size, field homogeneity, photon cross sections and photon spectra all contribute to this uncertainty.

The Monte Carlo calculated ionization chamber correction factors were all within 3% of unity. A detailed uncertainty analysis estimated the contributions of the field size, photon cross sections, photon spectra and chamber wall and central electrode dimensions to the uncertainty. The standard uncertainty on the calculated correction factors is 0.3% for all beam qualities. There are discrepancies between the calculated and measured chamber correction factors for all chambers. These discrepancies can be traced back to those between the measured and calculated absorbed dose to water-to-air kerma ratios. This might indicate that the PTB water calorimeter absorbed dose to water determination requires re-examination. Data from the BIPM kilovoltage primary standard, which uses Monte Carlo simulations, are consistent with the chamber correction factors calculated in this thesis. The correction factors calculated in this thesis also agree with those measured by several national metrological institutes (EURAMET.RI(I)-S13 and EURAMET.RI(I)-K9).

6.2 Future work

There are three possible avenues to explore further in relation to the work done for this thesis. They are listed here.

1. Calculate chamber correction factors for different field sizes. The correction factors calculated in this thesis are only applicable for field sizes 10 cm in diameter. The field size dependence of these factors, as shown in Table 4 of the TG-61 protocol [9], is not negligible. In order to perform reference dosimetry with the in-phantom method for different field sizes, data on chamber correction factors for these field sizes would be useful.

2. McGill University has access to its very own water calorimetry system [49, 74]. With the calorimetry system, it would be possible to perform absolute measurements of the absorbed dose to water in kilovoltage beams. Experimentally determined chamber correction factors could then be determined in the same fashion as PTB. It would be

interesting to compare the two sets of data, along with the calculated values from this thesis.

3. It would be ideal to determine which set of chamber correction factors are accurate; the PTB measured factors or the Monte Carlo calculated factors from this thesis. A simple experiment that would potentially point towards the more accurate set of factors would be to take the ratio of the correction factor at a given beam quality for two different chambers, $ch1$ and $ch2$. The ratio of the correction factors for the two chambers would then be

$$\frac{(P_{Q,cham})_{ch1}}{(P_{Q,cham})_{ch2}} = \frac{\left(\frac{\left(\frac{D_{w,z=2cm}}{K_a}\right)\left(\frac{M_a}{M_w}\right)}{\left[\left(\frac{\mu_{en}}{\rho}\right)_{w,a}\right]_{w,Q,z=2cm}}\right)_{ch1}}{\left(\frac{\left(\frac{D_{w,z=2cm}}{K_a}\right)\left(\frac{M_a}{M_w}\right)}{\left[\left(\frac{\mu_{en}}{\rho}\right)_{w,a}\right]_{w,Q,z=2cm}}\right)_{ch2}} = \frac{(M_a/M_w)_{ch1}}{(M_a/M_w)_{ch2}} \tag{6.1}$$

In Equation 6.1, the dose to water at a depth of 2 cm, the air kerma and the water-to-air mass-energy absorption coefficient ratio at a depth of 2 cm for the two chambers cancel out because they are chamber-independent factors. Experiments can be done to obtain the quantity on the right hand side of Equation 6.1. This quantity can then be compared to the correction factor ratio for the two chambers as determined with the MC (calculated) and PTB (experimental) data set. Whichever data set is closer to this quantity is possibly the more accurate set. Note that this method cannot be used to determine the actual values of the chamber correction factors.

References

9. Ma, C.-M. *et al.* AAPM protocol for 40–300 kV x-ray beam dosimetry in radiotherapy and radiobiology. *Medical Physics* **28(6),** 868–893 (2001).

49. Sarfehnia, A. *Water calorimetry-based radiation dosimetry in iridium-192 brachytherapy and proton therapy.* PhD diss. (McGill University, QC, 2010).

74. Renaud, J. *On the Development of Absorbed Dose Calorimeter Systems for Absolute Clinical Dosimetry.* PhD diss. (McGill University, QC, 2016).